Towards A Most Probable Recovery in Optical Imaging

Nadav Torem*, Roi Ronen*, Yoav Y. Schechner Viterbi Faculty of Electrical & Computer Eng. Technion, Haifa, Israel

torem@campus.technion.ac.il

Michael Elad Department of Computer Science Technion, Haifa, Israel

Abstract

Light is a complex-valued field. The intensity and phase of the field are affected by imaged objects. However, imaging sensors measure only real-valued non-negative intensities. This results in a nonlinear relation between the measurements and the unknown imaged objects. Moreover, the sensor readouts are corrupted by Poissonian-distributed photon noise. In this work, we seek the most probable object (or clear image), given noisy measurements, that is, maximizing the a-posteriori probability of the sought variables. Hence, we generalize annealed Langevin dynamics, tackling fundamental challenges in optical imaging, including phase recovery and Poisson (photon) denoising. We leverage deep neural networks, not for explicit recovery of the imaged object, but as an approximate gradient for a prior term. We show results on empirical data, acquired by a real experiment. We further show results of simulations. ¹

1. Introduction

Optical imaging relates to both the wave-nature and particle-nature of light. Due to the wave nature, light is a complex-valued field. The phase of the field is affected by objects, as well as propagation to and in the optical system. The phase of the complex-values wave is often important to recover [6], but image sensors measure only real-valued non-negative intensities. This leads to inverse problems such as phase-retrieval [13,45,47], ptychography [31], Fourier ptychography [33,41], and quantitative phase microscopy. These problems have a *nonlinear* relation between the measurements and the unknowns.

The particle nature leads to Poissonian-distributed photon noise in image readouts. Poisson noise complicates not only the said phase-related problems. It also complicates problems where image formation is linear, such as denois-

ing [12, 19], inpainting [17], deblurring, super-resolution, compressed sensing, and many other image recovery problems [2, 36, 39, 46, 48]. It of course complicates problems that are nonlinear [1,4,7,32,35,44] in the unknowns. In photon noise, variance increases with the expected measured intensities [27]. This noise model contradicts the most common assumption in signal processing, of a stationary Gaussian noise, whose variance is independent of the image content.

This paper addresses these general and fundamental traits of problems involving optical imaging. We wish to find the most probable object (or clear image), given image data, i.e., maximize the a-posteriori probability of the sought variables. In principle, maximization of this criterion, as any other differentiable criterion, can be the base for iterated gradient-based algorithms. This, however, would require that we know, preferably in analytic form, the probability distribution of real objects, given data. A method along these lines is called *Langevin dynamics* [30].

In practice, the probability of general objects given image data is unknown. We can only hope to approximate this probability and its gradient. An algorithm based such an approximation is termed *annealed Langevin dynamics*. It has shown great success in solving linear inverse problems having stationary, signal-independent Gaussian noise [14, 17, 42]. Our contribution here is in generalizing annealed Langevin dynamics to handle fundamental models of optical imaging, including phase recovery and Poisson (photon) noise.

Regarding alternatives that optimize solutions, we refer to two technologies. One of them broadly seeks a minimum of the mean squared error (MMSE) between recovered and original objects. Such methods tend to lead to blurred results, particularly if the noise is high. An underlying reason is that in high noise or in ill-posed problems, many potential solutions may equally explain the given data. Then, an MMSE estimator tends to an average solution, which is blurred. In contrast, maximization of the a-posteriori probability of the object seeks a specific solution that has a high

^{*}Equal contribution.

¹Our code will be released after peer-reviewed publication.

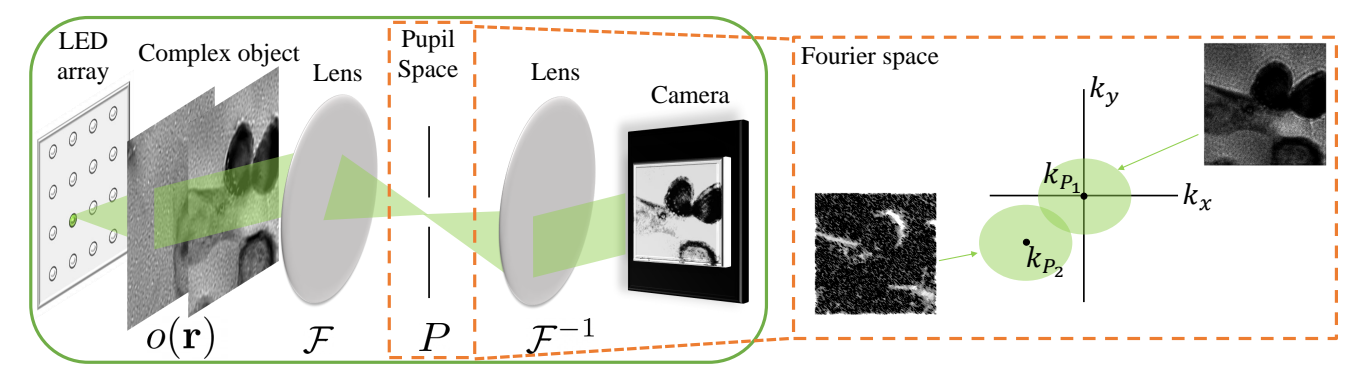


Figure 1. Imaging of a complex-valued object using a Fourier ptychography system. The object is projected to the frequency space and back to image space using the system optics. A camera measures the incoming light intensity, thus phase information is lost. The numerical aperture of the optical system sets the frequency support that is not filtered. It forms a 2D bandpass filter P, centered at spatial frequency k_m . Here, k_m is controlled by the illumination direction. By taking multiple images, illuminated from different directions, the Fourier space is scanned. The object amplitude and phase are recovered from these images.

probability, not an average over solutions. Hence, in our work, results can be as sharp and detailed as true objects.

The other technology is deep neural networks (DNNs), which can be trained to directly infer a solution given corrupted observations [8, 11, 15, 21, 22, 28, 29]. Sometimes, these DNNs form generative adversarial networks (GANs) [10]. However, DNNs tend to train on big data. Data size in some imaging modalities can be limited, particularly in images taken for scientific research. Moreover, DNNs are often trained along the MMSE criterion, while GAN-based algorithms sometimes tend [3, 26] to assume noiseless measurements. We leverage DNNs here, but not for explicit recovery of the clean object. Instead, we use DNNs to provide an approximate gradient for a prior term.

We show results on empirical data, acquired by a real experiment. We further show results of simulations.

2. Theoretical Background

2.1. Noise

Empirical light measurements are random, mainly due to the integer nature of photons and electric charges. This randomness is often regarded as photon noise. Dark noise, quantization noise, and photon noise are the dominant noise sources in common cameras [27]. Denote incorporation of noise into the expected signal $\mathbb I$ by the operator $\mathcal N$. The noisy measurement is

$$y = \mathcal{N}(\mathbf{I}) \ . \tag{1}$$

In this work, the model of \mathcal{N} contains only photon noise and quantization, the latter using 8 bits per pixel.

Photon noise is modeled by a Poisson process [27]. A pixel is characterized by its full well capacity (FWC), that is, the maximal amount of charge that can be accumulated in the pixel before saturating. Let $x^e \in [0, FWC]$ be the expected value of the measured signal (photo-electrons). The

corresponding noisy measurement is

$$y^{\rm e} \sim {\rm Poisson}(x^{\rm e}).$$
 (2)

2.2. Pseudo Poisson Distribution

Data analysis under Poisson noise is difficult to deal with in closed forms. Therefore, in many inverse problems, Poisson noise is approximated by a Gaussian distribution, $n^{\rm e} \sim N(0, x^{\rm e})$. Define normalized variables

$$x = \frac{x^e}{\text{FWC}} \in [0, 1] , \ y = \frac{y^e}{\text{FWC}} , \ \sigma_0 = \frac{1}{\sqrt{\text{FWC}}} .$$
 (3)

The Gaussian approximation of a measurement is

$$n^{\text{meas}} \sim N(0, \sigma_0^2 x) . \tag{4}$$

The normalized approximation of Eq. (2) is

$$y \approx x + n^{\text{meas}}$$
 (5)

In Eqs. (2) and (5), the noise variance depends linearly on x, and the signal-to-noise-ratio (SNR) is the same. Hence, in this work, the parameter σ_0 controls the measurement noise level

2.3. Nonlinear Imaging: Complex-valued Objects

Let \mathbf{r} represent the 2D spatial coordinate of an object. Let $a(\mathbf{r})$, $\phi(\mathbf{r})$ be its amplitude and phase, respectively, and $j=\sqrt{-1}$. An optically-thin object has transmittance $o(\mathbf{r})=a(\mathbf{r})\exp{[j\phi(\mathbf{r})]}$. Cameras only measure intensity. Therefore, optical imaging systems can often be formulated by an imaging model, which is nonlinear in o. Let ρ be the object irradiance. Let H be a linear transformation, which depends on the optical system. A noisy measurement y is modeled by

$$y = \mathcal{N}\left(\rho |H\{o(\mathbf{r})\}|^2\right) . \tag{6}$$

For example, in the phase retrieval problem [34], H is equivalent to the Fourier transform \mathcal{F} .

Fourier ptychography, illustrated in Fig. 1, uses a set of M linear transformations $H = \{H_m\}_{m=1}^M$. This method enables to expand the diffraction limit set by the numerical aperture of the optical system, thus increasing the optical resolution. Let \mathcal{F}^{-1} be the inverse Fourier transform. In the spatial frequency domain \mathbf{k} , the pupil function $P(\mathbf{k} - \mathbf{k}_m)$ is a 2D bandpass filter, centered at spatial frequency \mathbf{k}_m with a spatial bandwidth set by the system numerical aperture. Overall,

$$H_m\{o(\mathbf{r})\} = \mathcal{F}^{-1}\{P(\mathbf{k} - \mathbf{k}_m)\mathcal{F}\{o(\mathbf{r})\}\}.$$
 (7)

Discretize $o(\mathbf{r})$ to q elements and the measurements $y(\mathbf{r})$ to $q^{\mathrm{meas}} = Mq$ sampled pixels, creating vectors $\mathbf{o} \in \mathbb{C}^q$ and $\mathbf{y} \in \mathbb{R}^{q^{\mathrm{meas}}}$. The discrete version of the linear transformation H is $\mathbf{H} \in \mathbb{C}^{q^{\mathrm{meas}} \times q}$. The discrete versions of the Fourier transform, its inverse, and the pupil function are denoted by $\mathbf{F}, \mathbf{F}^{-1}, \mathbf{P}_m \in \mathbb{C}^{q \times q}$, respectively. Then, $\mathbf{H}_m \mathbf{o} = \sqrt{\rho} \mathbf{F}^{-1} \left[\mathbf{P}_m \odot \left[\mathbf{Fo} \right] \right]$, where \odot is an element-wise multiplication. Assume that the dominant noise in Eq. (6) is photon noise. Following Sec. 2.2, during data analysis, we approximate this noise as Gaussian $\mathbf{n}^{\mathrm{meas}} \sim N(0, \sigma_0^2 |\mathbf{Ho}|^2)$. Then, Eq. (6) takes the form

$$\mathbf{y} = |\mathbf{Ho}|^2 + \mathbf{n}^{\text{meas}} . \tag{8}$$

2.4. MMSE Denoiser

Consider Gaussian noise $\mathbf{w} \sim N(0, \sigma^2 \mathbf{I})$, where \mathbf{I} is the identity matrix. Let

$$\mathbf{x}' = \mathbf{x} + \mathbf{w} \tag{9}$$

be a noisy version of a clean image \mathbf{x} . Here, \mathbf{x}' may be noisy data \mathbf{y} , or an artificially corrupted version of \mathbf{x} . Let $D^{\mathrm{Gauss}}(\mathbf{x}'|\sigma)$ be an estimate of \mathbf{x} obtained by a minimum mean squared error (MMSE) denoiser, that is designed for Gaussian noise. Then,

$$D^{\text{Gauss}}(\mathbf{x}'|\sigma) = \arg\min_{D} \mathbb{E}\left[\|D(\mathbf{x}'|\sigma) - \mathbf{x}\|_{2}^{2} \right]$$
 (10)

The gradient [14] of the log probability $\nabla_{\mathbf{x}'} \log p(\mathbf{x}')$ of a noisy image has a property that will become handy:

$$\nabla_{\mathbf{x}'} \log p(\mathbf{x}') = \frac{D^{\text{Gauss}}(\mathbf{x}'|\sigma) - \mathbf{x}'}{\sigma^2} . \tag{11}$$

Denoising is ill-posed: a noisy input may have multiple possible solutions. An MMSE denoiser tends to average these possible outcomes [17]. In a high-noise scenario, such averaging often leads to output images with blurry edges and unclear fine details. To address this, Refs. [16, 17] suggest denoising using *Langevin dynamics*, converging stochastically to a single sharp possible solution.

2.5. Langevin Dynamics

Let $t \in [1, \dots, T]$ be an iteration index and $\alpha_t > 0$ be an appropriately chosen small function of t, having $\alpha_{t \to T} = 0$. The following iterations should converge to a solution that maximizes the probability distribution $p(\mathbf{x}|\mathbf{y})$

$$\mathbf{x}_{t+1} = \mathbf{x}_t + \alpha_t \nabla_{\mathbf{x}_t} \log p(\mathbf{x}_t | \mathbf{y}) . \tag{12}$$

Eq. (12) may converge to an undesired local maximum of the distribution $p(\mathbf{x}|\mathbf{y})$. To address that, Langevin dynamics [43] adds to Eq. (12) synthetic noise $\mathbf{n}_t^{\mathrm{Langevin}} \sim N(0, \mathbf{I})$ at iteration t,

$$\mathbf{x}_{t+1} = \mathbf{x}_t + \alpha_t \nabla_{\mathbf{x}_t} \log p(\mathbf{x}_t | \mathbf{y}) + \sqrt{2\alpha_t} \mathbf{n}_t^{\text{Langevin}}$$
. (13)

In general, when solving an inverse problem, neither $p(\mathbf{x}_t|\mathbf{y})$ nor $\nabla_{\mathbf{x}_t}\log p(\mathbf{x}_t|\mathbf{y})$ are known. Still, to use Eq. (13), there is a need to assess $\nabla_{\mathbf{x}_t}\log p(\mathbf{x}_t|\mathbf{y})$. To address that, Ref. [37] extends Eq. (13) into annealed Langevin dynamics. Hence, iterations would not perform Eq. (13), and would not attempt to update a vector \mathbf{x}_t whose probability cannot be computed. Instead, iterations would update a vector, that we denote $\tilde{\mathbf{x}}_t$, for which we can analytically assess the gradient $\nabla_{\tilde{\mathbf{x}}_t}\log p(\tilde{\mathbf{x}}_t|\mathbf{y})$. We thus need to properly define $\tilde{\mathbf{x}}_t$. Analogously to Eq. (13), annealed Langevin dynamics has this iterative rule

$$\tilde{\mathbf{x}}_{t+1} = \tilde{\mathbf{x}}_t + \alpha_t \nabla_{\tilde{\mathbf{x}}_t} \log p(\tilde{\mathbf{x}}_t | \mathbf{y}) + \sqrt{2\alpha_t} \mathbf{n}_t^{\text{Langevin}}$$
. (14)

Any $\tilde{\mathbf{x}}_t$ differs from \mathbf{x} by an error $\mathbf{e}_t^{\text{annea}}$,

$$\tilde{\mathbf{x}}_t = \mathbf{x} + \mathbf{e}_t^{\text{annea}} \,. \tag{15}$$

We stress that this induced error $\mathbf{e}_t^{\mathrm{annea}}$ is only a conceptual mathematical maneuver, and is not actually added during the iterative process. It is important that the probability distribution of $\mathbf{e}_t^{\mathrm{annea}}$ would be known, despite not knowing the actual value of $\mathbf{e}_t^{\mathrm{annea}}$. Moreover, the error is designed such that $\mathbf{e}_{t \to T}^{\mathrm{annea}} \approx 0$. For example, Refs. [16, 17] stochastically solve the following linear inverse problems of the form $\mathbf{y} = \mathbf{H}\mathbf{x} + \mathbf{w}$, which generalizes Eq. (9). At iteration t, they suggest $\mathbf{e}_t^{\mathrm{annea}} \sim N(0, \sigma_t^2 \mathbf{I})$, to suit the noise distribution of \mathbf{w} . At t = 1, $\mathbf{e}_t^{\mathrm{annea}}$ has a high standard deviation σ_t . Gradually, this standard deviation reduces to near zero.

Let us proceed with the description of annealed Langevin dynamics (14). Using Bayes rule,

$$\nabla_{\tilde{\mathbf{x}}_t} \log p(\tilde{\mathbf{x}}_t | \mathbf{y}) = \nabla_{\tilde{\mathbf{x}}_t} \left[\log p(\mathbf{y} | \tilde{\mathbf{x}}_t) + \log p(\tilde{\mathbf{x}}_t) \right] . \quad (16)$$

There is a need to derive tractable expressions to the right-hand side of Eq. (16). The term $\nabla_{\tilde{\mathbf{x}}_t} \log p(\mathbf{y}|\tilde{\mathbf{x}}_t)$ in Eq. (16) can sometimes be derived analytically using the known distribution of $\mathbf{e}_t^{\text{annea}}$, as we show in Secs. 3.1 and 3.2. Refs. [16, 17] rely on Eq. (11) to assess $\nabla_{\tilde{\mathbf{x}}_t} \log p(\tilde{\mathbf{x}}_t)$. Before imaging takes place, they pre-train a DNN to approximate $D^{\text{Gauss}}(\mathbf{x}'|\sigma)$, using synthetic pairs of clean and

noisy images $(\mathbf{x}, \mathbf{x}')$. They follow [38], to train a network $h_{\Theta}^{\text{Gauss}}(\mathbf{x}'|\sigma)$ having learnable parameters Θ that predicts directly the relative noise $(\mathbf{x} - \mathbf{x}')/\sigma^2$, such that

$$\hat{\Theta} = \arg\min_{\Theta} \mathbb{E} \left[\left\| \frac{\mathbf{x} - \mathbf{x}'}{\sigma^2} - h_{\Theta}^{\text{Gauss}}(\mathbf{x}'|\sigma) \right\|_2^2 \right] . \quad (17)$$

Here, the expectation \mathbb{E} is approximated as an empirical average of all pairs in the training set of clean and noisy images $(\mathbf{x}, \mathbf{x}')$. Then,

$$\nabla_{\mathbf{x}'} \log p(\mathbf{x}') \approx h_{\Theta}^{\text{Gauss}}(\mathbf{x}'|\sigma)$$
 (18)

3. Langevin Dynamics for Nonlinearity

As described in Secs. 2.1 and 2.3, real-world imaging models and measurements have: (a) Poisson distributed noise; (b) Nonlinear transforms over complex-valued objects. Hence, there is a need to extend annealed Langevin dynamics for both cases (a) and (b).

3.1. Denoising Poissonian Image Intensities

We now attempt to recover an image x, given its noisy version y. As discussed in Sec. 2.1, y contains several types of noise. Indeed data is *generated* using a rich noise model. For *data analysis*, however, we act as if y is related by Eq. (5). The parameter σ_0 is known from the camera properties by Eq. (3), as described in Sec. 2.2. Here, all vector operations are *element-wise*. Analogously to [16,17], we set a sequence of noise levels $\sigma_0 > \sigma_1 \ge \sigma_2 \ge \cdots \ge \sigma_T = 0$, and $\sum_{\tau=1}^T \sigma_\tau^2 = \sigma_0^2$. Let e_t^{part} be a statistically independent synthetic *partial* dummy error term, distributed as

$$\mathbf{e}_t^{\text{part}} \sim N\left[0, (\sigma_t^2 - \sigma_{t+1}^2)\mathbf{I}\right]$$
 (19)

A sum of zero-mean Gaussian variables is a Gaussian, whose variance is the sum of the variances. So,

$$\sum_{\tau=t_1}^{t_2} \mathbf{e}_{\tau}^{\text{part}} \sim N\left[0, (\sigma_{t_1}^2 - \sigma_{t_2}^2)\mathbf{I}\right] . \tag{20}$$

Using Eqs. (4) and (20), we design e_t^{part} such that

$$\mathbf{n}^{\text{meas}} = \sqrt{\mathbf{x}} \sum_{\tau=0}^{T} \mathbf{e}_{\tau}^{\text{part}} . \tag{21}$$

Moreover, recall that $\mathbf{e}_t^{\mathrm{annea}}$ is a dummy error term. We set $\mathbf{e}_t^{\mathrm{annea}}$ in this task as

$$\mathbf{e}_t^{\mathrm{annea}} = \sum_{t}^{T} \mathbf{e}_{\tau}^{\mathrm{part}} \ . \tag{22}$$

We do *not* set $\mathbf{e}_t^{\text{annea}}$ as in Sec. 2.5 because the noise in Sec. 2.5 has stationary Gaussian distribution and here it is Poissonian (signal-dependent).

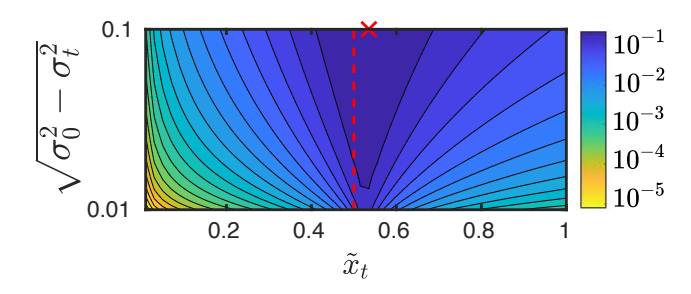


Figure 2. A visualization in log scale of the probability in Eq. (26). Here x=0.5 is a scalar, depicted by a red dashed line, while y is its noisy version obtained by Eq. (5) with $\sigma_0=0.1$. The red cross marker depicts the probability maximum.

We generalize Eq. (15) to Poisson noise, by defining an annealed variable

$$\tilde{\mathbf{x}}_t = \mathbf{x} + \sqrt{\mathbf{x}}\mathbf{e}_t^{\text{annea}} = \mathbf{x} + \sqrt{\mathbf{x}}\sum_{\tau=t}^T \mathbf{e}_{\tau}^{\text{part}}$$
. (23)

Eq. (23) allows us to derive $\nabla_{\tilde{\mathbf{x}}_t} \log p(\mathbf{y}|\tilde{\mathbf{x}}_t)$ analytically for Poisson denoising. Inserting Eqs. (21) and (23) in Eq. (5) yields

$$\mathbf{y} = \tilde{\mathbf{x}}_t - \sqrt{\mathbf{x}} \sum_{\tau=t}^T \mathbf{e}_{\tau}^{\text{part}} + \sqrt{\mathbf{x}} \sum_{\tau=0}^T \mathbf{e}_{\tau}^{\text{part}} = \tilde{\mathbf{x}}_t + \sqrt{\mathbf{x}} \sum_{\tau=0}^{t-1} \mathbf{e}_{\tau}^{\text{part}}.$$
(24)

Notice that $\tilde{\mathbf{x}}_t$ is statistically independent of the additional dummy error $\sum_{\tau=0}^{t-1} \mathbf{e}_{\tau}^{\mathrm{part}}$. Thus, from Eqs. (20) and (24),

$$p(\mathbf{y}|\tilde{\mathbf{x}}_t) = p\left(\sqrt{\mathbf{x}}\sum_{\tau=0}^{t-1}\mathbf{e}_{\tau}^{\text{part}}\right)$$
$$= \frac{1}{\sqrt{2\pi(\sigma_0^2 - \sigma_t^2)\mathbf{x}}}\exp\left(-\frac{(\mathbf{y} - \tilde{\mathbf{x}}_t)^2}{2(\sigma_0^2 - \sigma_t^2)\mathbf{x}}\right). \tag{25}$$

However, \mathbf{x} in Eq. (25) is unknown. Therefore, to set a covariance in Eq. (25), we make an approximation² $\mathbf{x} \approx \tilde{\mathbf{x}}_t$. This approximation *is applied only in Eq.* (25), skewing there the covariance. We do not use $\tilde{\mathbf{x}}_t$ as a denoised version yet.³ Overall, the approximated probability is

$$p(\mathbf{y}|\tilde{\mathbf{x}}_t) \approx \frac{1}{\sqrt{2\pi(\sigma_0^2 - \sigma_t^2)\tilde{\mathbf{x}}_t}} \exp\left(-\frac{(\mathbf{y} - \tilde{\mathbf{x}}_t)^2}{2(\sigma_0^2 - \sigma_t^2)\tilde{\mathbf{x}}_t}\right).$$
 (26)

In Fig. 2, we visualize Eq. (26). Computing the gradient of the logarithm of Eq. (26) results in

$$\nabla_{\tilde{\mathbf{x}}_t} \log p(\mathbf{y}|\tilde{\mathbf{x}}_t) = \frac{1}{2(\sigma_0^2 - \sigma_t^2)} \left(\frac{\mathbf{y}^2}{\tilde{\mathbf{x}}_t^2} - 1\right) - \frac{1}{2\tilde{\mathbf{x}}_t} . (27)$$

²Here, $\nabla_{\tilde{\mathbf{x}}_t} \log p(\mathbf{y}|\tilde{\mathbf{x}}_t)$ cannot be derived analytically. We detail this point in Appendix A.1.

³Note that from Eq. (22) when $t \to T$ then $\mathbf{e}_t^{\text{annea}} \to 0$.

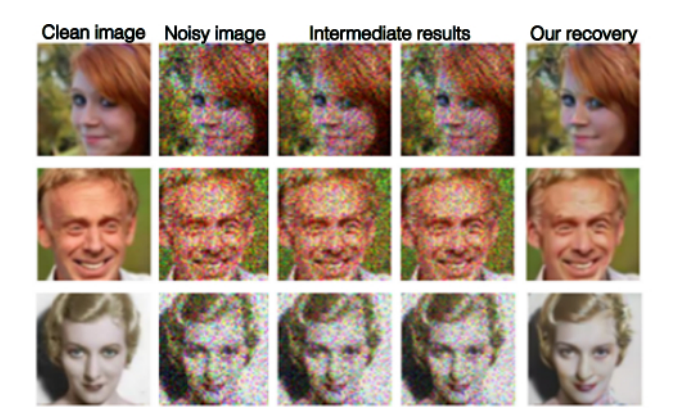


Figure 3. Poisson denoising by our method in Sec. 3.1, for $\sigma_0 = 0.3$

In analogy to Eq. (11), we compute $\nabla_{\tilde{\mathbf{x}}_t} \log p(\tilde{\mathbf{x}}_t)$. The derivation is detailed in Appendix A.2. Here we bring the final result. Let $D^{\text{Poisson}}(\mathbf{x}'|\sigma)$ be an MMSE *Poisson* denoiser of a corrupted image \mathbf{x}' , created from a clean image \mathbf{x} using Eqs. (3), (4), and (5) by noise level σ . Then,

$$\nabla_{\mathbf{x}'} \log p(\mathbf{x}') = \frac{D^{\text{Poisson}}(\mathbf{x}'|\sigma) - \mathbf{x}'}{\sigma^2 \sqrt{\mathbf{x}}}.$$
 (28)

We do not have D^{Poisson} . So, before imaging takes place, we pre-train a DNN $h_{\Theta}^{\mathrm{Poisson}}$ having learnable parameters Θ to approximate D^{Poisson} using synthetic pairs of clean and noisy images $(\mathbf{x}, \mathbf{x}')$,

$$\hat{\Theta} = \arg\min_{\Theta} \mathbb{E} \left[\left\| \frac{\mathbf{x} - \mathbf{x}'}{\sigma^2 \mathbf{x}} - h_{\Theta}^{\text{Poisson}}(\mathbf{x}' | \sigma) \right\|_2^2 \right] . \quad (29)$$

Here, the expectation \mathbb{E} is approximated as an empirical average of all pairs in the training set of clean and noisy images $(\mathbf{x}, \mathbf{x}')$. Note the analogy of Eq. (17) and Eq. (29): the difference originates from the noise distributions, Gaussian versus Poissonian. Overall, using Eqs. (16), (27), (28) and (29)

$$\nabla_{\tilde{\mathbf{x}}_{t}} \log p(\tilde{\mathbf{x}}_{t}|\mathbf{y}) = \frac{1}{2(\sigma_{0}^{2} - \sigma_{t}^{2})} \left(\frac{\mathbf{y}^{2}}{\tilde{\mathbf{x}}_{t}^{2}} - 1\right) - \frac{1}{2\tilde{\mathbf{x}}_{t}} + h_{\hat{\Theta}}^{\text{Poisson}}(\tilde{\mathbf{x}}_{t}|\sigma_{t}) . \quad (30)$$

The iterative algorithm is described in Algorithm 1. Fig. 3 shows intermediate and final qualitative results of our annealed Langevin dynamics for Poisson denoising.

3.2. Recovering Complex-Valued Objects

In this section, we formulate annealed Langevin dynamics for nonlinear imaging models, as described in Sec. 2.3. Let $\Re(\cdot)$, $\Im(\cdot)$ be real and imaginary arguments of a complex-valued number, respectively. Analogously to Eq. (13), for Langevin dynamics, $\nabla_{\mathbf{o}_t} \log p(\mathbf{o}_t|\mathbf{y})$ is

needed. However, $p(\mathbf{o}_t|\mathbf{y})$ is not known, thus analogously to Eq. (14), annealed Langevin dynamics for a complex-valued object is

$$\tilde{\mathbf{o}}_{t+1} = \tilde{\mathbf{o}}_t + \alpha_t \nabla_{\tilde{\mathbf{o}}_t} \log p(\tilde{\mathbf{o}}_t | \mathbf{y}) + \sqrt{2\alpha_t} \mathbf{n}_t^{\text{Langevin}}$$
. (31)

Here, $\mathbf{n}^{\mathrm{Langevin}}$ is a random complex-valued vector, where $\Re(\mathbf{n}^{\mathrm{Langevin}})$, $\Im(\mathbf{n}^{\mathrm{Langevin}}) \sim N(0,\mathbf{I})$ and independent. For simplicity, we present here the special case $\mathbf{H} = \mathbf{I}$ in Eq. (8). Thus, most derivations can be given in scalar formulation, that is, $y = |o|^2 + n^{\mathrm{meas}}$. The generalization of the model to a general \mathbf{H} is detailed in Appendix \mathbf{B} . Analogously to Eq. (15), we set

$$\tilde{o}_t = o + e_t^{\text{annea}} \,. \tag{32}$$

Using Eq. (32) in Eq. (8) yields

$$y = |\tilde{o}_t|^2 - e_t^{\text{couple}} + |e_t^{\text{annea}}|^2 + n^{\text{meas}},$$
 (33)

where

$$|o_t|^2 = \Re(o_t)^2 + \Im(o_t)^2$$
, (34)

$$e_t^{\text{couple}} = 2 \left[\Re(\tilde{o}_t) \Re(e_t^{\text{annea}}) + \Im(\tilde{o}_t) \Im(e_t^{\text{annea}}) \right], \quad (35)$$

and

$$|e_t^{\text{annea}}|^2 = \Re(e_t^{\text{annea}})^2 + \Im(e_t^{\text{annea}})^2$$
. (36)

The non-linearity of Eq. (8) yields in two terms in Eq. (33) that pose analytic challenges: a coupling term of $e_t^{\rm couple}$; and a squared annealing error term $|e_t^{\rm annea}|^2$. We handle them by introducing a *relaxed* model, creating nonlinear annealed Langevin dynamics for complex-valued objects, as

$$y = |\tilde{o}_t|^2 - e_t^{\text{couple}} + |e_t^{\text{annea}}|^2 + \tilde{n}_t^{\text{meas}} - \sigma_t^2 z_t . \quad (37)$$

We detail Eq. (37) and specifically e_t^{annea} , $\tilde{n}_t^{\text{meas}}$ and z_t in Sec. 3.2.1.

3.2.1 Relaxation of the Nonlinear Problem

Let $\{\sigma_t\}_{t=0}^T$ be a sequence of standard deviations, set to $\sigma_0 > \sigma_1 \ge \sigma_2 \ge \cdots \ge \sigma_T = 0$, and $\sum_{\tau=1}^T \sigma_\tau^2 = \sigma_0^2$. Let

$$\Re(e_t^{\text{part}}), \Im(e_t^{\text{part}}) \sim N[0, \frac{1}{4}(\sigma_t^2 - \sigma_{t+1}^2)]$$
 (38)

be statistically independent Gaussian variables. As described in Sec. 2.3 and in Eq. (4), for $\mathbf{H} = \mathbf{I}$, $n^{\text{meas}} \sim N(0, \sigma_0^2 |o|^2)$. Using $|o|^2$ from Eq. (34), $n^{\text{meas}} \sim N[0, \sigma_0^2 \Re(o)^2 + \sigma_0^2 \Im(o)^2]$. In analogy to Eq. (21), we use Eq. (38) and design dummy variables $\Re(e_t^{\text{part}}), \Im(e_t^{\text{part}})$ such that,

$$n^{\text{meas}} = 2\Re(o) \sum_{\tau=0}^{T} \Re(e_{\tau}^{\text{part}}) + 2\Im(o) \sum_{\tau=0}^{T} \Im(e_{\tau}^{\text{part}})$$
. (39)

Notice that Eq. (39) now has a form similar to the coupling term e_t^{couple} in Eq. (35). To make computations tractable, we assume $o \approx \tilde{o}_t$ in Eq. (39). We do not use \tilde{o}_t as a denoised version yet. An approximate⁴ measurement noise is

$$\tilde{n}_t^{\text{meas}} = 2\Re(\tilde{o}_t) \sum_{\tau=0}^T \Re(e_{\tau}^{\text{part}}) + 2\Im(\tilde{o}_t) \sum_{i=0}^T \Im(e_{\tau}^{\text{part}}) .$$
(40)

We now detail z_t that appears Eq. (37). Here, z_t is designed to address the challenge of a squared annealing error term $|e_t^{\text{annea}}|^2$. Therefore, we generalize the annealing error in Eq. (22) to a *complex-valued* annealing error,

$$e_t^{\text{annea}} = \sum_{\tau=t}^{T} \left[\Re(e_{\tau}^{\text{part}}) + j \Im(e_{\tau}^{\text{part}}) \right]. \tag{41}$$

Thus,

$$|e_t^{\text{annea}}|^2 = \left[\sum_{\tau=t}^T \Re(e_{\tau}^{\text{part}})\right]^2 + \left[\sum_{\tau=t}^T \Im(e_{\tau}^{\text{part}})\right]^2 . \quad (42)$$

A chi-squared distribution $\chi^2(\kappa)$ is defined by a sum of κ random variables: each independent, having a square-normal distribution [20]. So, $|e_t^{\rm annea}|^2$ in Eq. (42) is distributed $\chi^2(2)$, up to scale. Analogously to $|e_t^{\rm annea}|^2$, we propose two annealing error terms accordingly,⁵

$$z_{t \to T} = \frac{\left[\sum_{\tau=t}^{T} \Re(e_{\tau}^{\text{part}})\right]^{2}}{\sigma_{t}^{2}} + \frac{\left[\sum_{\tau=t}^{T} \Im(e_{\tau}^{\text{part}})\right]^{2}}{\sigma_{t}^{2}}, \quad (43)$$

and

$$z_{0\to(t-1)} = \frac{\left[\sum_{\tau=0}^{t-1} \Re(e_{\tau}^{\text{part}})\right]^2}{\sigma_t^2} + \frac{\left[\sum_{\tau=0}^{t-1} \Im(e_{\tau}^{\text{part}})\right]^2}{\sigma_t^2} \ . \tag{44}$$

So, $z_{0\to(t-1)}, z_{t\to T}$ in Eqs. (43) and (44) are distributed $\chi^2(2)$, up to scale. Then using Eqs. (43) and (44), we define

$$z_t = z_{t \to T} - z_{0 \to (t-1)} . {45}$$

Using Eqs. (35) and (40), define

 $e_t^{\text{remain}}(\tilde{o}_t) = \tilde{n}_t^{\text{meas}} - e_t^{\text{couple}}$

$$= 2\Re(\tilde{o}_t) \sum_{\tau=0}^{t-1} \Re(e_{\tau}^{\text{part}}) + 2\Im(\tilde{o}_t) \sum_{\tau=0}^{t-1} \Im(e_{\tau}^{\text{part}}) . \tag{46}$$

Using Eqs. (42) and (45), define

$$z_t^{\text{remain}} = |e_t^{\text{annea}}|^2 - \sigma_t^2 z_t$$

$$= \left[\sum_{\tau=0}^{t-1} \Re(e_{\tau}^{\text{part}}) \right]^2 + \left[\sum_{\tau=0}^{t-1} \Im(e_{\tau}^{\text{part}}) \right]^2. \tag{47}$$

Insert Eqs. (46) and (47) into the relaxed model in Eq. (37). This yields

$$y = |\tilde{o}_t|^2 + e_t^{\text{remain}}(\tilde{o}_t) + z_t^{\text{remain}}. \tag{48}$$

Using Eq. (48), $\nabla_{\tilde{o}_t} \log p(y|\tilde{o}_t)$ can be derived analytically. Here we give the final results, the derivation is detailed in Appendix B.1. Let I_0 , I_1 be the modified Bessel functions of the first kind [5]. Let

$$\mathcal{I}(\tilde{o}_t, y) = I_1 \left(\frac{|\tilde{o}_t| \sqrt{y}}{\sigma_0^2 - \sigma_t^2} \right) / I_0 \left(\frac{|\tilde{o}_t| \sqrt{y}}{\sigma_0^2 - \sigma_t^2} \right). \tag{49}$$

Then,

$$\nabla_{\tilde{o}_t} \log p(y|\tilde{o}_t) = \frac{\tilde{o}_t}{2(\sigma_0^2 - \sigma_t^2)} \left[\mathcal{I}(\tilde{o}_t, y) \frac{\sqrt{y}}{|\tilde{o}_t|} - 1 \right]. \quad (50)$$

Equivalently to Eq. (11), we compute $\nabla_{\tilde{\mathbf{o}}_t} \log p(\tilde{\mathbf{o}}_t)$. The derivation is detailed in Appendix B.2. Let $D^{\mathrm{complex}}(\mathbf{o}'|\sigma)$ be the MMSE Gaussian denoiser for a noisy complex-valued object \mathbf{o}' that had been created by a clean object \mathbf{o} . Here, $\Re(\mathbf{o}'), \Im(\mathbf{o}')$ are corrupted by independent Gaussian noise vectors, each having noise level σ . The gradient $\nabla_{\mathbf{o}'} \log p(\mathbf{o}')$ is given by $\nabla_{\mathbf{o}'} \log p(\mathbf{o}') = [D^{\mathrm{complex}}(\mathbf{o}'|\sigma) - \mathbf{o}']/\sigma^2$. We do not have D^{complex} . Hence again, before imaging takes place, we pre-train a DNN $h_{\Theta}^{\mathrm{complex}}$ having learnable parameters Θ to approximate $\nabla_{\mathbf{o}'} \log p(\mathbf{o}')$, using synthetic pairs of clean and noisy complex-valued objects $(\mathbf{o}, \mathbf{o}')$,

$$\hat{\Theta} = \arg\min_{\Theta} \mathbb{E} \left[\left\| \frac{\mathbf{o} - \mathbf{o}'}{\sigma^2} - h_{\Theta}^{\text{complex}}(\mathbf{o}'|\sigma) \right\|_2^2 \right] . \quad (51)$$

Here, the expectation \mathbb{E} is approximated as an empirical average of all pairs in the training set of clean and noisy complex-valued objects $(\mathbf{o}, \mathbf{o}')$. Overall, the iterative algorithm is described in Algorithm 1.

4. Examples

All tests set the DNN denoiser using the NCSNv2 architecture [38]. Let \mathbf{x} , $\hat{\mathbf{x}}$ be the ground-truth and estimated images. We evaluate the results using

$$MSE(\hat{\mathbf{x}}) = \|\mathbf{x} - \hat{\mathbf{x}}\|_{2}^{2} / q,$$

$$PSNR(\hat{\mathbf{x}}) = 10 \log_{10} \left([MSE(\hat{\mathbf{x}})]^{-1} \right).$$
 (52)

For complex-valued objects, the amplitude is evaluated by Eq. (52). Let \angle o be the phase of a complex-valued o. Note that there is an inherent phase ambiguity due to the $|\cdot|^2$ operation and the periodicity of 2π . Therefore, we evaluate

⁴From Eq. (32), the approximation becomes accurate as $e_t^{\rm annea} \to 0$, where $\tilde{o}_t \to o$ and $\tilde{n}_t^{\rm meas} \to n^{\rm meas}$.

⁵Note that $\sigma_t^2 z_t$ in Eq. (37) can be considered as an additional annealing error in the measurement domain.

⁶The network input is a two-channel tensor of $\Re(\mathbf{o}')$, $\Im(\mathbf{o}')$.

Algorithm 1: Langevin dynamics for complexvalued objects. For real-valued images, $\tilde{\mathbf{o}}$ is replaced by $\tilde{\mathbf{x}}$

Input:
$$\{\sigma_t\}_{t=1}^T, \mathbf{y} | \sigma_0 \text{ and a small constant } \epsilon$$
Initialize $\tilde{\mathbf{o}}_0$, e.g. Gaussian noise, \mathbf{y} , or HIO

for $t \leftarrow 1$ to T do

$$\alpha_t \leftarrow \epsilon \frac{\sigma_t^2}{\sigma_T^2}$$
Draw $\mathbf{n}_t^{\text{Langevin}}$ from a Gaussian distribution

if $\tilde{\mathbf{o}}$ is complex-valued then

From Eq. (50) compute gradient
$$\Delta_t \leftarrow \nabla_{\tilde{\mathbf{o}}_{t-1}} \log p(\mathbf{y} | \tilde{\mathbf{o}}_{t-1}) + h_{\hat{\Theta}}^{\text{complex}}(\tilde{\mathbf{o}}_{t-1} | \sigma_t)$$
else
$$| \text{From Eq. (30) compute gradient} | \Delta_t \leftarrow \nabla_{\tilde{\mathbf{o}}_{t-1}} \log p(\mathbf{y} | \tilde{\mathbf{o}}_{t-1}) + h_{\hat{\Theta}}^{\text{Poisson}}(\tilde{\mathbf{o}}_{t-1} | \sigma_t)$$
end
$$\tilde{\mathbf{o}}_t \leftarrow \tilde{\mathbf{o}}_{t-1} + \alpha_t \Delta_t + \sqrt{2\alpha_t} \mathbf{n}_t^{\text{Langevin}}$$
end
$$\tilde{\mathbf{o}}_t \leftarrow \tilde{\mathbf{o}}_{t-1} + \alpha_t \Delta_t + \sqrt{2\alpha_t} \mathbf{n}_t^{\text{Langevin}}$$

σ_0	MMSE solution	Ours
0.05	38.1 ± 1.1	36.9 ± 0.9
0.10	34.5 ± 1.1	33.1 ± 0.9
0.20	30.6 ± 1.1	28.7 ± 1.3
0.30	28.5 ± 1.2	25.9 ± 1.4
0.40	27.2 ± 1.2	23.8 ± 1.8

Table 1. PSNR (Eq. 52) results for Poisson denoising, using 50 images of the CelebA test set.

phase recovery by

$$\begin{aligned} \text{MSE}^{\text{phase}}(\angle \hat{\mathbf{o}}) &= \arg\min_{\theta} \left\| \angle \mathbf{o} - \left(\angle \hat{\mathbf{o}} + \theta \right) \right\|_{2}^{2} / q \;, \\ \text{PSNR}^{\text{phase}}(\angle \hat{\mathbf{o}}) &= 10 \log_{10} \left[(2\pi)^{2} \left[\text{MSE}^{\text{phase}}(\angle \hat{\mathbf{o}}) \right]^{-1} \right] \;. \end{aligned} \tag{53}$$

The CelebA dataset of faces, each of size 64×64 pixels, is corrupted by Poisson noise (not pseudo-gaussian noise) characterized by noise level σ_0 . Moreover, each image channel also undergoes quantization using 8 bits per pixel before being normalized to the range [0,1].

4.1. Denoising Poissonian Image Intensities

We demonstrate our approach described in Sec. 3.1. Per image on RTX 3090 GPU, the denoising runtime is ~ 1 minute. Fig. 4 and Tab. 1 compare our results with an MMSE solution, that is, $\hat{\mathbf{x}}^{\text{MMSE}} = \mathbf{y} - h_{\Theta}^{\text{Poisson}}(\mathbf{y}|\sigma_0)$. Our denoised images have higher quality than the MMSE results, which have blur. This trend is preserved across images and different noise levels. More examples are shown in Appendix D.1.

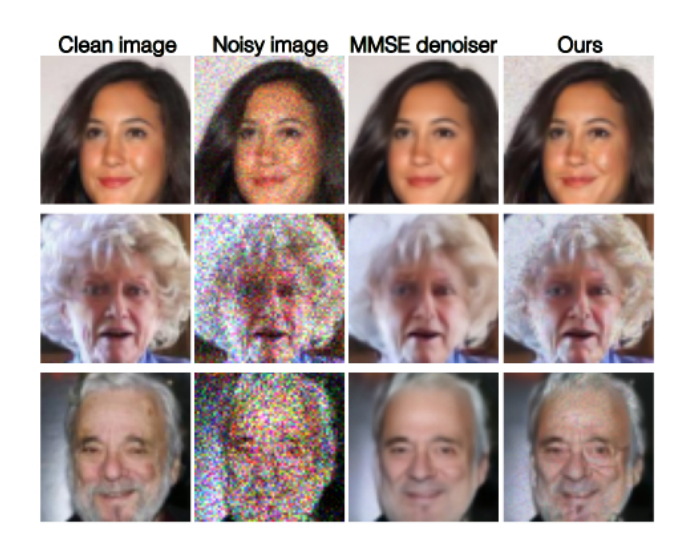


Figure 4. Poisson denoising results. The rows correspond to noise levels $\sigma_0 = \{0.1, 0.2, 0.3\}$. MMSE denoised results have blur.

We then follow the approach of [17] and assess if the estimated image holds $\hat{\mathbf{x}} \sim p(\mathbf{x})$. Denote a color channel by $\mathbf{c} \in \{R,G,B\}$, a pixel index by $\mathbf{p} \in [1,q^{\text{meas}}]$, and a test image index by $i \in [1,N^{\text{set}}]$. Define a relative error of channel \mathbf{c} , pixel \mathbf{p} and image i by $\hat{n}^{\text{rel}}_{\text{c,p}}(i) \equiv [y_{\text{c,p}}(i) - \hat{x}_{\text{c,p}}(i)] / \sqrt{\hat{x}_{\text{c,p}}(i)}$. Using Eqs. (4) and (5), assessing $\hat{\mathbf{x}} \sim p(\mathbf{x})$ can be done by verifying if a relative error image $\hat{\mathbf{n}}^{\text{rel}} = [(\mathbf{y} - \hat{\mathbf{x}}) / \sqrt{\hat{\mathbf{x}}}]$ is distributed as $N(0, \sigma_0^2 \mathbf{I})$. As shown in Fig. 5, the distribution of $\hat{n}^{\text{rel}}_{\text{c,p}}$ seems indeed white and Gaussian. Let us assess the mean and variance of $\hat{n}^{\text{rel}}_{\text{c,p}}$.

Per i, the mean and the root mean squared relative errors are, respectively,

$$\mu_{\rm rel}(i) = \frac{1}{3q^{\rm meas}} \sum_{\rm p=1}^{q^{\rm meas}} \sum_{\rm c=1}^{3} \hat{n}_{\rm c,p}^{\rm rel}(i) ,$$

$$\sigma_{\rm rel}(i) = \sqrt{\frac{1}{3q^{\rm meas}}} \sum_{\rm p=1}^{q^{\rm meas}} \sum_{\rm c=1}^{3} [\hat{n}_{\rm c,p}^{\rm rel}(i)]^{2} . \tag{54}$$

We ran our method to denoise $N^{\rm set}=50$ images from the CelebA test set. For all denoised images, we computed $\hat{\mathbf{n}}^{\rm rel}(i)$ for $i\in[1,N^{\rm set}]$ and calculated $\mu_{\rm rel}(i)$, $\sigma_{\rm rel}(i)$, using Eq. (54). In our experiment, for each characterized noise level σ_0 and $\forall i,\ \mu_{\rm rel}(i)\approx 0$. The distribution statistics of $\sigma_{\rm rel}(i)$ appear in Fig. 6, including its empirical average over the test set, that is,

$$\hat{\sigma} = \frac{1}{N^{\text{set}}} \sum_{i=1}^{N^{\text{set}}} \sigma_{\text{rel}}(i) . \tag{55}$$

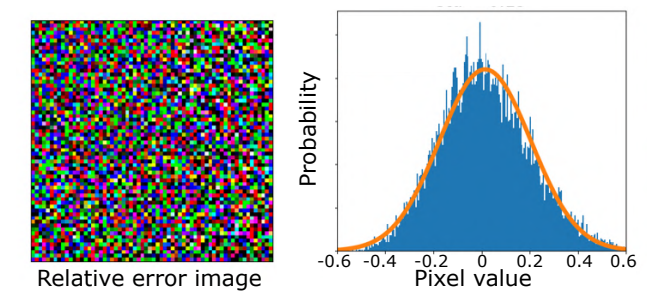


Figure 5. [Left] The relative error image $\hat{\mathbf{n}}^{\rm rel}$, following our recovery using data corrupted by $\sigma_0=0.2$. [Right] Normalized histogram of $\hat{n}_{\rm c,p}^{\rm rel}$. The orange line is a Gaussian curve, using the spatial mean and standard deviation $\mu_{\rm rel}$, $\sigma_{\rm rel}$, obtained by Eq. (54). Here, $\mu_{\rm rel}\approx 0$, and $\sigma_{\rm rel}=0.19$.

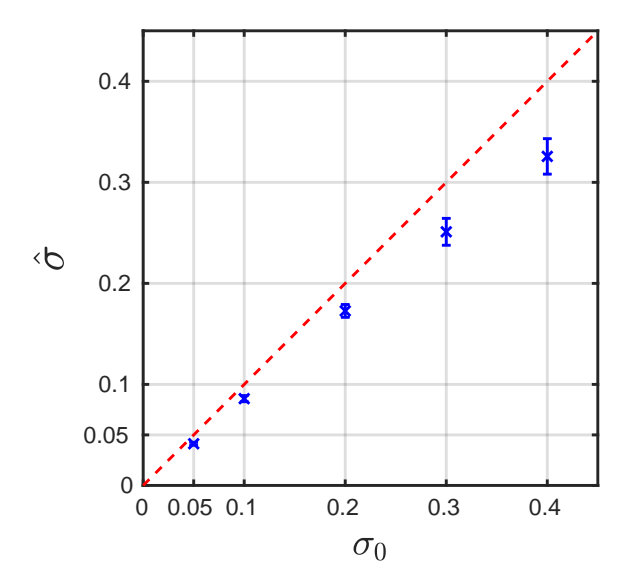


Figure 6. The blue crosses denote $\hat{\sigma}$ (Eq. 55), for different characterized noise levels σ_0 . The dashed red line represents a perfect estimation.

4.2. Phase Retrieval

As described in Sec. 2.3, phase retrieval can be modeled using $\mathbf{H} = \mathbf{F}$, that is, $\mathbf{y} = |\mathbf{F}\mathbf{x}|^2$. Note that even if \mathbf{x} is a real-valued image, the measurement \mathbf{y} lacks phase information. This task is ill-posed. The Hybrid Input-Output (HIO) [9] algorithm is frequently used in phase retrieval. Let ψ be a random Gaussian vector. HIO initializes hundreds of possible candidate solutions $\{\mathbf{x}_l\}$ by $\mathbf{F}\mathbf{x}_l = \sqrt{\mathbf{y}}\exp(j2\pi\psi_l)$. Then, HIO iteratively uses negative feedback in Fourier space, in order to progressively force the candidate solutions to conform to the problem constraints. The candidate that holds best these constraints is the evaluated HIO solution. Fig. 7 compares our method, described in Sec. 3.2, with HIO on the CelebA test set. Here, we initialize our algorithm with an extremely noisy

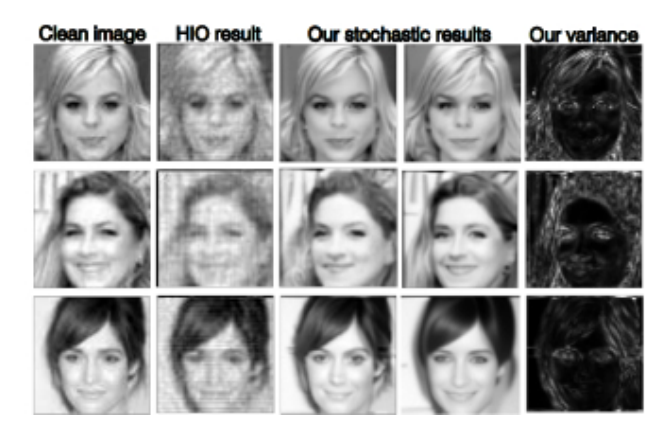


Figure 7. Phase retrieval results. The variance image is obtained by using 50 random initializations of Algorithm 1.

version of the HIO solution. We found that it gives us better robustness during convergence, but still stochastically converges to a variety of possible solutions, having high perceptual quality, as presented in Fig. 7. We show additional phase retrieval results in Appendix D.2.

4.3. Fourier Ptychography: Real Experiment

We further demonstrate our approach on the Fourier ptychography problem, described in Sec. 2.3 and in Fig. 1. We use data of real-world publicly available complex-valued biological samples [40]. Using a Fourier ptychography imaging system, the amplitude and phase of a sample of human bone cells are recovered [41]. We randomly divided the recovered sample into non-spatially overlapping patches, each of size 256×256 pixels. Then, the patches were split randomly into training and test sets. We train our denoiser over the training set, according to Eq. (51). For each patch o in the test set, we simulate M noisy measured images, each corresponding to a single LED, according to Eqs. (6) and (7). Fig. 8 shows the results using Algorithm 1. There are two interesting points that arise from Fig. 8: (i) For a large number of LED measurements, M=89, the phase recovery quality is insensitive to the noise level. (ii) There is a leap in phase recovery when the number of measurements is greater than ~ 50 . This may be caused by a better coverage of Fourier space using shifted bands. We show additional qualitative and quantitative results in Appendix D.3.

5. Discussion

We generalize annealed Langevin dynamics to realistic optical imaging, which involves complex-valued objects and Poisson noise. Our method is generic and can be applied to a variety of imaging transformations \mathbf{H} . Furthermore, the pre-trained DNN denoiser in Eq. (51) is independent of specific imaging system parameters σ_0 and \mathbf{H} of

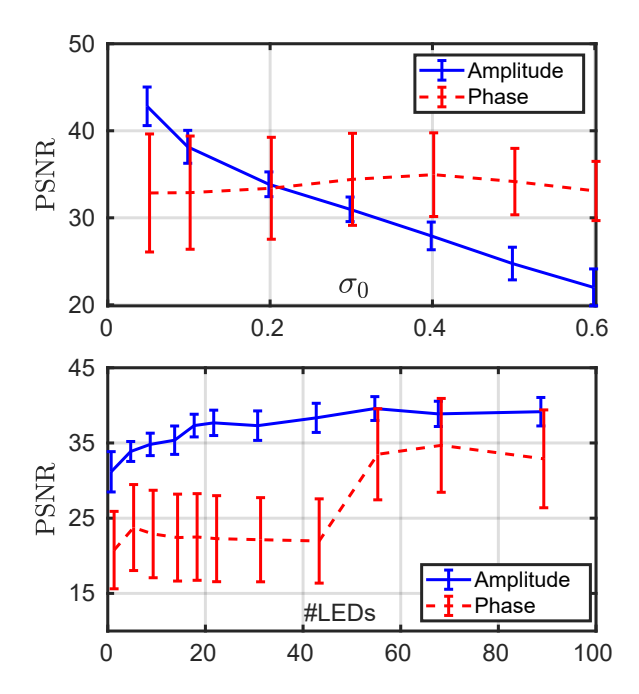


Figure 8. The average PSNR of 10 complex-valued objects: [Top] For different Poisson noise levels σ_0 , and M=89. [Bottum] For a varying number of LEDs M and a fixed noise level $\sigma_0=0.1$. The bars stand for the PSNR standard deviation.

Eq. (8). Hence, the same DNN denoiser can be used for various optical systems.

Dealing with strong non-Gaussian noise is essential in real-world imaging. Effects such as quantization noise or dead-time noise in SPAD-based imagers have very different statistical properties. So, noise statistics create new and interesting challenges, specifically in low-light conditions. Therefore, motivated by this paper, we hope that more research expands annealed Langevin dynamics to additional challenging models of real noise statistics, better approaching a most probable recovery result.

There are more challenging forward models in imaging. These include imaging by coherent illumination (with speckles), partial-coherence, and models that are nonlinear with respect to the illumination (e.g. two-photon microscopy). Other computer vision problems are highly nonlinear in the unknonws, such as tomography scatter fields. So, there is a lot of room to contribute to computational vision and imaging by expanding this work.

Acknowledgment

We thank Laura Waller and Lei Tian for pointing us to the data in [40,41]. We are grateful to Ashok Veeraraghavan and Christopher A. Metzler for referring us to the publicly available source code of [24]. We cherish the technical support of Johanan Erez, Ina Talmon, and Daniel Yagodin. Yoav Schechner is the Mark and Diane Seiden Chair in Science at the Technion. He is a Landau Fellow - supported by the Taub Foundation. His work was conducted in the Ollendorff Minerva Center. Minvera is funded through the BMBF.

Appendix

A. Denoising Poissonian Image Intensities

This section details the complete derivations in Sec. 3.1. To be self-contained, this section repeats some equations that already exist in Sec. 3.1. In this section, all vector operations are *element-wise*. Denote incorporation of noise into a clean image x by the operator \mathcal{N} . The noisy measurement is

$$\mathbf{y} = \mathcal{N}(\mathbf{x}) . \tag{56}$$

Let $N(0, \sigma^2)$ be a Gaussian distribution with zero expectation and variance σ^2 . Let σ_0 be a noise level, known from the camera properties, as described in Sec. 2.2. We set a sequence of noise levels

$$\sigma_0 > \sigma_1 \ge \sigma_2 \ge \dots \ge \sigma_T = 0$$
, (57)

which satisfies

$$\sum_{t=1}^{T} \sigma_t^2 = \sigma_0^2 \ . \tag{58}$$

For analysis, we act as if y is related by Eq. (5),

$$\mathbf{y} = \mathbf{x} + \mathbf{n}^{\text{meas}} , \tag{59}$$

where

$$\mathbf{n}^{\text{meas}} \sim N(0, \sigma_0^2 \mathbf{x}) = \sqrt{\mathbf{x}} N(0, \sigma_0^2 \mathbf{I}) , \qquad (60)$$

and I is the identity matrix.

Recall from Sec. 2.5 that $t \in [1, ..., T]$ is an iteration index, and $\alpha_t > 0$ is an appropriately chosen small function of t. Annealed Langevin dynamics has this iterative rule

$$\tilde{\mathbf{x}}_{t+1} = \tilde{\mathbf{x}}_t + \alpha_t \nabla_{\tilde{\mathbf{x}}_t} \log p(\tilde{\mathbf{x}}_t | \mathbf{y}) + \sqrt{2\alpha_t} \mathbf{n}_t^{\text{Langevin}}$$
. (61)

Using Bayes rule,

$$\nabla_{\tilde{\mathbf{x}}_t} \log p(\tilde{\mathbf{x}}_t | \mathbf{y}) = \nabla_{\tilde{\mathbf{x}}_t} \left[\log p(\mathbf{y} | \tilde{\mathbf{x}}_t) + \log p(\tilde{\mathbf{x}}_t) \right] .$$
 (62)

Here, $\mathbf{n}_t^{\text{Langevin}} \sim N(0, \mathbf{I})$ is *synthetic* noise at iteration t.

In Appendix A.1, we detail $\nabla_{\tilde{\mathbf{x}}_t} \log p(\mathbf{y}|\tilde{\mathbf{x}}_t)$, while $\nabla_{\tilde{\mathbf{x}}_t} \log p(\tilde{\mathbf{x}}_t)$ is described in Appendix A.2. Overall, the algorithm for Langevin dynamics for denoising Poissonian image intensities is shown in Algorithm 2. The small constant ϵ in Algorithm 2 is a pre-defined step size.

A.1. Likelihood Gradient: Poisson Denoising

Let $\mathbf{e}_t^{\mathrm{part}}$ be a statistically independent synthetic *partial* dummy error term, distributed as

$$\mathbf{e}_t^{\text{part}} \sim N\left[0, (\sigma_t^2 - \sigma_{t+1}^2)\mathbf{I}\right]$$
 (63)

Algorithm 2: Langevin dynamics for denoising Poissonian image intensities

Input: $\{\sigma_t\}_{t=1}^T, \mathbf{y}, \sigma_0 \text{ and a small constant } \epsilon$ Initialize $\tilde{\mathbf{x}}_0 \sim N(0, \sigma_0^2 \mathbf{I})$ for $t \leftarrow 1$ to T do

$$\begin{split} & \boldsymbol{\epsilon} \leftarrow 1 \text{ to } I \text{ do} \\ & \alpha_t \leftarrow \epsilon \frac{\sigma_t^2}{\sigma_T^2} \\ & \text{Draw } \mathbf{n}_t^{\text{Langevin}} \sim N(0, \mathbf{I}) \\ & \text{From Eq. (88) compute gradient:} \\ & \boldsymbol{\Delta}_t \leftarrow \nabla_{\tilde{\mathbf{x}}_{t-1}} \log p(\mathbf{y}|\tilde{\mathbf{x}}_{t-1}) + h_{\hat{\boldsymbol{\Theta}}}^{\text{Poisson}}(\tilde{\mathbf{x}}_{t-1}|\sigma_t) \\ & \tilde{\mathbf{x}}_t \leftarrow \tilde{\mathbf{x}}_{t-1} + \alpha_t \boldsymbol{\Delta}_t + \sqrt{2\alpha_t} \mathbf{n}_t^{\text{Langevin}} \end{split}$$

end

$$\hat{\mathbf{x}} \leftarrow \tilde{\mathbf{x}}_T$$

A sum of zero-mean Gaussian variables is a Gaussian, whose variance is the sum of the variances. So,

$$\sum_{\tau=t_{1}}^{t_{2}} \mathbf{e}_{\tau}^{\text{part}} \sim N \left[0, \sum_{\tau=t_{1}}^{t_{2}} (\sigma_{\tau}^{2} - \sigma_{\tau+1}^{2}) \mathbf{I} \right] = N \left[0, (\sigma_{t_{1}}^{2} - \sigma_{t_{2}}^{2}) \mathbf{I} \right] . (64)$$

Note that using Eqs. (57), (58) and (64)

$$\sum_{\tau=0}^{T} \mathbf{e}_{\tau}^{\text{part}} \sim N\left(0, \sigma_0^2 \mathbf{I}\right) . \tag{65}$$

Using Eqs. (60) and (65), we design epart such that

$$\mathbf{n}^{\text{meas}} = \sqrt{\mathbf{x}} N(0, \sigma_0^2 \mathbf{I}) = \sqrt{\mathbf{x}} \sum_{\tau=0}^T \mathbf{e}_{\tau}^{\text{part}} .$$
 (66)

Let $\mathbf{e}_t^{\mathrm{annea}}$ be a dummy error term. We design $\mathbf{e}_t^{\mathrm{annea}}$ such that it is contained in the measurement noise. This enables to derive an analytical approximate expression for $\nabla_{\mathbf{\tilde{x}}_t} \log p(\mathbf{y}|\mathbf{\tilde{x}}_t)$. We set

$$\mathbf{e}_t^{\text{annea}} = \sum_{\tau=t}^T \mathbf{e}_{\tau}^{\text{part}} . \tag{67}$$

We further define the dummy error by a relation between the unknown desired variable x and annealed variable,

$$\mathbf{e}_t^{\text{annea}} = \frac{\tilde{\mathbf{x}}_t - \mathbf{x}}{\sqrt{\mathbf{x}}} \ . \tag{68}$$

Using Eqs. (67) and (68),

$$\tilde{\mathbf{x}}_t = \mathbf{x} + \sqrt{\mathbf{x}} \mathbf{e}_t^{\text{annea}} = \tilde{\mathbf{x}}_t + \sqrt{\mathbf{x}} \sum_{\tau = t}^T \mathbf{e}_{\tau}^{\text{part}}$$
 (69)

Inserting Eqs. (66) and (69) in Eq. (59) yields

$$\mathbf{y} = \tilde{\mathbf{x}}_t - \sqrt{\mathbf{x}} \sum_{\tau=t}^T \mathbf{e}_{\tau}^{\text{part}} + \sqrt{\mathbf{x}} \sum_{\tau=0}^T \mathbf{e}_{\tau}^{\text{part}} = \tilde{\mathbf{x}}_t + \sqrt{\mathbf{x}} \sum_{\tau=0}^{t-1} \mathbf{e}_{\tau}^{\text{part}}.$$
(70)

To derive $\nabla_{\tilde{\mathbf{x}}_t} \log p(\mathbf{y}|\tilde{\mathbf{x}}_t)$, we seek to express \mathbf{y} using terms (besides $\tilde{\mathbf{x}}_t$) whose probability distributions are known and independent of $\tilde{\mathbf{x}}_t$. However, in Eq. (70), \mathbf{x} is unknown. We can hypothetically extract \mathbf{x} from Eq. (69) using

$$\mathbf{x} = \frac{1}{2} \left[2\tilde{\mathbf{x}}_t \pm \sqrt{4\tilde{\mathbf{x}}_t + (\mathbf{e}_t^{\text{annea}})^2} \mathbf{e}_t^{\text{annea}} + (\mathbf{e}_t^{\text{annea}})^2 \right],$$
(71)

and substitute Eq. (71) in Eq. (70). This would make y expressed using three terms: \tilde{x}_t , e_t^{annea} and $\sum_{\tau=0}^{t-1} e_{\tau}^{part}$. However, from Eq. (69), \tilde{x}_t , e_t^{annea} are statistically dependent. Thus, we cannot use Eq. (71).

Instead, we apply the following steps. From Eqs. (64) and (70),

$$p(\mathbf{y}|\tilde{\mathbf{x}}_t) = p\left(\sqrt{\mathbf{x}}\sum_{\tau=0}^{t-1}\mathbf{e}_{\tau}^{\text{part}}\right)$$

$$= \frac{1}{\sqrt{2\pi(\sigma_0^2 - \sigma_t^2)\mathbf{x}}} \exp\left[-\frac{(\mathbf{y} - \tilde{\mathbf{x}}_t)^2}{2(\sigma_0^2 - \sigma_t^2)\mathbf{x}}\right]. \tag{72}$$

Recall that \mathbf{x} in Eq. (72) is unknown. Therefore, to set a covariance in Eq. (72), we make an approximation $\mathbf{x} \approx \tilde{\mathbf{x}}_t$. This approximation is applied only in Eq. (72). We do not yet use $\tilde{\mathbf{x}}_t$ as a denoised version. It is not yet a recovery attempt. The approximation only handles the covariance in Eq. (72), skewing it. Overall, the approximated probability distribution function is

$$p(\mathbf{y}|\tilde{\mathbf{x}}_t) \approx \frac{1}{\sqrt{2\pi(\sigma_0^2 - \sigma_t^2)\tilde{\mathbf{x}}_t}} \exp\left[-\frac{(\mathbf{y} - \tilde{\mathbf{x}}_t)^2}{2(\sigma_0^2 - \sigma_t^2)\tilde{\mathbf{x}}_t}\right]. \quad (73)$$

Computing the gradient of the logarithm of Eq. (73) results in

$$\nabla_{\tilde{\mathbf{x}}_t} \log p(\mathbf{y}|\tilde{\mathbf{x}}_t) = \frac{1}{2(\sigma_0^2 - \sigma_t^2)} \left(\frac{\mathbf{y}^2}{\tilde{\mathbf{x}}_t^2} - 1\right) - \frac{1}{2\tilde{\mathbf{x}}_t} . \tag{74}$$

A.2. Gradient of the Prior: Poisson Denoising

We need to derive $\nabla_{\tilde{\mathbf{x}}_t} \log p(\tilde{\mathbf{x}}_t)$ in Eq. (62) for iterations of annealed Langevin dynamics. So, before imaging takes place, we pre-train a deep neural network (DNN) $h_{\Theta}^{\mathrm{Poisson}}$, to approximate $\nabla_{\tilde{\mathbf{x}}_t} \log p(\tilde{\mathbf{x}}_t)$. This process is described in this section.

In analogy to Eq. (69), let (x, x') be a synthetic pair of clean and noisy images, rendered using

$$\mathbf{x}' = \mathbf{x} + \sqrt{\mathbf{x}} \mathbf{n}^{\text{train}} . \tag{75}$$

Here, $\mathbf{n}^{\text{train}} \sim N(0, \sigma^2 \mathbf{I})$, where σ is an arbitrary noise level. Using Eq. (75),

$$p(\mathbf{x}'|\mathbf{x}) = p(\mathbf{x}' - \mathbf{x}|\mathbf{x}) = p(\sqrt{\mathbf{x}}\mathbf{n}^{\text{train}}|\mathbf{x})$$
$$= \frac{1}{\sqrt{2\pi\sigma^2\mathbf{x}}} \exp\left[-\frac{(\mathbf{x}' - \mathbf{x})^2}{2\sigma^2\mathbf{x}}\right]. \quad (76)$$

By definition, the marginal distribution $p(\mathbf{x}')$ can be written as,

$$p(\mathbf{x}') = \int p(\mathbf{x}'|\mathbf{x})p(\mathbf{x})d\mathbf{x}.$$
 (77)

Inserting Eq. (76) in Eq. (77) yields

$$p(\mathbf{x}') = \int \frac{1}{\sqrt{2\pi\sigma^2 \mathbf{x}}} \exp\left[-\frac{(\mathbf{x}' - \mathbf{x})^2}{2\sigma^2 \mathbf{x}}\right] p(\mathbf{x}) d\mathbf{x} . \quad (78)$$

Then, the gradient of Eq. (78) satisfies

$$\nabla_{\mathbf{x}'} p(\mathbf{x}') = \int \frac{1}{\sqrt{2\pi\sigma^2 \mathbf{x}}} \nabla_{\mathbf{x}'} \exp\left[-\frac{(\mathbf{x}' - \mathbf{x})^2}{2\sigma^2 \mathbf{x}}\right] p(\mathbf{x}) d\mathbf{x}$$
$$= \int \left[\frac{\mathbf{x} - \mathbf{x}'}{\sigma^2 \mathbf{x}}\right] \frac{1}{\sqrt{2\pi\sigma^2 \mathbf{x}}} \exp\left[-\frac{(\mathbf{x}' - \mathbf{x})^2}{2\sigma^2 \mathbf{x}}\right] p(\mathbf{x}) d\mathbf{x} . \tag{79}$$

Insert the definition of $p(\mathbf{x}'|\mathbf{x})$ given in Eq. (76) into Eq. (79). This results in

$$\nabla_{\mathbf{x}'} p(\mathbf{x}') = \int \left[\frac{\mathbf{x} - \tilde{\mathbf{x}}}{\sigma^2 \mathbf{x}} \right] p(\mathbf{x}' | \mathbf{x}) p(\mathbf{x}) d\mathbf{x} . \tag{80}$$

Divide both sides of Eq. (80) by $p(\mathbf{x}')$. This leads to

$$\frac{\nabla_{\mathbf{x}'}p(\mathbf{x}')}{p(\mathbf{x}')} = \int \left[\frac{\mathbf{x} - \tilde{\mathbf{x}}}{\sigma^2 \mathbf{x}}\right] \frac{p(\mathbf{x}'|\mathbf{x})p(\mathbf{x})}{p(\mathbf{x}')} d\mathbf{x} . \tag{81}$$

Recall Bayes rule,

$$p(\mathbf{x}|\mathbf{x}') = \frac{p(\mathbf{x}'|\mathbf{x})p(\mathbf{x})}{p(\mathbf{x}')}.$$
 (82)

Insert Eq. (82) in Eq. (81). This results in

$$\frac{\nabla_{\mathbf{x}'}p(\mathbf{x}')}{p(\mathbf{x}')} = \int \left[\frac{\mathbf{x} - \tilde{\mathbf{x}}}{\sigma^2 \mathbf{x}}\right] p(\mathbf{x}|\mathbf{x}') d\mathbf{x} . \tag{83}$$

The left-hand side of Eq. (83) satisfies

$$\frac{\nabla_{\mathbf{x}'} p(\mathbf{x}')}{p(\mathbf{x}')} = \nabla_{\mathbf{x}'} \log p(\tilde{\mathbf{x}}) . \tag{84}$$

The right-hand side of Eq. (83) can be written as

$$\int \left[\frac{\mathbf{x} - \mathbf{x}'}{\sigma^2 \mathbf{x}} \right] p(\mathbf{x} | \mathbf{x}') d\mathbf{x} = \mathbb{E} \left[\frac{\mathbf{x} - \mathbf{x}'}{\sigma^2 \mathbf{x}} | \mathbf{x}' \right] , \qquad (85)$$

where \mathbb{E} denotes expectation. Overall, from Eqs. (83) to (85),

$$\nabla_{\mathbf{x}'} \log p(\mathbf{x}') = \mathbb{E} \left[\frac{\mathbf{x} - \mathbf{x}'}{\sigma^2 \mathbf{x}} \middle| \mathbf{x}' \right] . \tag{86}$$

The expectation in Eq. (86) cannot be calculated analytically. The reason is that the probability distribution of \mathbf{x} is not accessible. Therefore, we approximate the expectation in Eq. (86) using a DNN. We generate a large dataset of synthetic pairs of clean and noisy images $(\mathbf{x}, \mathbf{x}')$ using Eq. (75), with various standard deviations σ . Then, we train a deep neural network $h_{\Theta}^{\text{Poisson}}(\mathbf{x}'|\sigma)$ having learnable parameters Θ , such that

$$\hat{\Theta} = \arg\min_{\Theta} \mathbb{E} \left[\left\| \frac{\mathbf{x} - \mathbf{x}'}{\sigma^2 \mathbf{x}} - h_{\Theta}^{\text{Poisson}}(\mathbf{x}' | \sigma) \right\|_2^2 \right] . \quad (87)$$

Here, the expectation \mathbb{E} is approximated as an empirical average of all pairs in the training set of clean and noisy images $(\mathbf{x}, \mathbf{x}')$. Overall, using Eqs. (62), (74), (86) and (87)

$$\nabla_{\tilde{\mathbf{x}}_{t}} \log p(\tilde{\mathbf{x}}_{t}|\mathbf{y}) = \frac{1}{2(\sigma_{0}^{2} - \sigma_{t}^{2})} \left(\frac{\mathbf{y}^{2}}{\tilde{\mathbf{x}}_{t}^{2}} - 1\right) - \frac{1}{2\tilde{\mathbf{x}}_{t}} + h_{\hat{\Theta}}^{\text{Poisson}}(\tilde{\mathbf{x}}_{t}|\sigma_{t}) . \quad (88)$$

B. Recovering Complex-Valued Objects

This section details the complete derivations of annealed Langevin dynamics for nonlinear imaging models, described in Sec. 3.2. To be self-contained, this section repeats some equations that already exist in Sec. 3.2. Here, a noisy measurement satisfies

$$\mathbf{v} = \mathcal{N}(|\mathbf{Ho}|^2) \,, \tag{89}$$

where across this paper, $|\cdot|^2$ operates element-wise. For analysis, we act as if y is related by Eq. (8), that is,

$$\mathbf{y} = |\mathbf{Ho}|^2 + \mathbf{n}^{\text{meas}} , \qquad (90)$$

where

$$\mathbf{n}^{\text{meas}} \sim N(0, \sigma_0^2 |\mathbf{Ho}|^2)$$
. (91)

Let $\Re(\cdot)$, $\Im(\cdot)$ be real and imaginary arguments of a complex-valued number, respectively. By definition

$$|\mathbf{Ho}|^2 = \left[\Re(\mathbf{Ho})\right]^2 + \left[\Im(\mathbf{Ho})\right]^2. \tag{92}$$

From Eqs. (91) and (92), we obtain

$$\mathbf{n}^{\text{meas}} \sim N(0, \sigma_0^2 |\mathbf{Ho}|^2)$$

$$= N\left(0, \sigma_0^2 [\Re(\mathbf{Ho})]^2 + \sigma_0^2 \Im[(\mathbf{Ho})]^2\right) . \tag{93}$$

Analogously to Eq. (61), annealed Langevin dynamics for a complex-valued object is

$$\tilde{\mathbf{o}}_{t+1} = \tilde{\mathbf{o}}_t + \alpha_t \nabla_{\tilde{\mathbf{o}}_t} \log p(\tilde{\mathbf{o}}_t | \mathbf{y}) + \sqrt{2\alpha_t} \mathbf{n}_t^{\text{Langevin}}$$
. (94)

Here, $\Re(\mathbf{n}^{\text{Langevin}})$, $\Im(\mathbf{n}^{\text{Langevin}}) \sim N(0, \mathbf{I})$, distributed independently. Using Bayes rule,

$$\nabla_{\tilde{\mathbf{o}}_t} \log p(\tilde{\mathbf{o}}_t | \mathbf{y}) = \nabla_{\tilde{\mathbf{o}}_t} \left[\log p(\mathbf{y} | \tilde{\mathbf{o}}_t) + \log p(\tilde{\mathbf{o}}_t) \right] . \quad (95)$$

Algorithm 3: Langevin dynamics for complex-valued objects.

Input: $\{\sigma_t\}_{t=1}^T, \mathbf{y}, \mathbf{H}, \sigma_0 \text{ and a small constant } \epsilon$ Initialize $\tilde{\mathbf{o}}_0$, e.g. by Gaussian noise, or by \mathbf{y} for $t \leftarrow 1$ to T do $\begin{vmatrix} \alpha_t \leftarrow \epsilon \frac{\sigma_t^2}{\sigma_T^2} \\ Draw \ \mathbf{n}_t^{\mathrm{Langevin}} = N(0, \mathbf{I}) + jN(0, \mathbf{I}) \\ From \ \mathrm{Eq.} \ (151) \ \mathrm{compute} \ \mathrm{gradient:} \\ \Delta_t \leftarrow \nabla_{\tilde{\mathbf{o}}_{t-1}} \log p(\mathbf{y}|\tilde{\mathbf{o}}_{t-1}) + h_{\hat{\Theta}}^{\mathrm{complex}}(\tilde{\mathbf{o}}_{t-1}|\sigma_t) \\ \tilde{\mathbf{o}}_t \leftarrow \tilde{\mathbf{o}}_{t-1} + \alpha_t \Delta_t + \sqrt{2\alpha_t} \mathbf{n}_t^{\mathrm{Langevin}} \\ \mathbf{end} \\ \hat{\mathbf{o}} \leftarrow \tilde{\mathbf{o}}_T$

In Appendix B.1 we detail $\nabla_{\tilde{\mathbf{o}}_t} \log p(\mathbf{y}|\tilde{\mathbf{o}}_t)$, while $\nabla_{\tilde{\mathbf{o}}_t} \log p(\tilde{\mathbf{o}}_t)$ is described in Appendix B.2. Overall, the algorithm for Langevin dynamics for complex-valued objects is shown in Algorithm 3. The small constant ϵ in Algorithm 3 is a pre-defined step size.

B.1. Likelihood Gradient: Complex-Valued Objects

Sec. 3.2 summarizes the special case $\mathbf{H} = \mathbf{I}$ in Eq. (90). Here, nevertheless, we detail the derivations for a general \mathbf{H} matrix. In analogy to Eq. (67), here we define a *complex-valued* dummy error term $\mathbf{e}_t^{\text{annea}}$. Regardless of the exact value of $\mathbf{e}_t^{\text{annea}}$, which is given in Appendix B.1.1, we set

$$\mathbf{e}_t^{\text{annea}} = \tilde{\mathbf{o}}_t - \mathbf{o} . \tag{96}$$

By definition

$$|\mathbf{Ho}_t|^2 = \left[\Re(\mathbf{Ho}_t)\right]^2 + \left[\Im(\mathbf{Ho}_t)\right]^2 , \qquad (97)$$

and

$$|\mathbf{H}\mathbf{e}_t^{\text{annea}}|^2 = \left[\Re(\mathbf{H}\mathbf{e}_t^{\text{annea}})\right]^2 + \left[\Im(\mathbf{H}\mathbf{e}_t^{\text{annea}})\right]^2 \ . \tag{98}$$

Let ⊙ denote an element-wise product. Define

$$\mathbf{e}_{t}^{\text{couple}} = 2\Re(\mathbf{H}\tilde{\mathbf{o}}_{t}) \odot \Re(\mathbf{H}\mathbf{e}_{t}^{\text{annea}}) + 2\Im(\mathbf{H}\tilde{\mathbf{o}}_{t}) \odot \Im(\mathbf{H}\mathbf{e}_{t}^{\text{annea}}).$$
(99)

Using Eqs. (96), (97), (98), and (99), $|Ho|^2$ satisfies

$$|\mathbf{Ho}|^{2} = |\mathbf{H}(\tilde{\mathbf{o}}_{t} - \mathbf{e}_{t}^{\text{annea}})|^{2} = |\mathbf{H}\tilde{\mathbf{o}}_{t} - \mathbf{H}\mathbf{e}_{t}^{\text{annea}}|^{2}$$

$$= [\Re(\mathbf{H}\tilde{\mathbf{o}}_{t}) - \Re(\mathbf{H}\mathbf{e}_{t}^{\text{annea}})]^{2} + [\Im(\mathbf{H}\tilde{\mathbf{o}}_{t}) - \Im(\mathbf{H}\mathbf{e}_{t}^{\text{annea}})]^{2}$$

$$= |\mathbf{H}\tilde{\mathbf{o}}_{t}|^{2} - \mathbf{e}_{t}^{\text{couple}} + |\mathbf{H}\mathbf{e}_{t}^{\text{annea}}|^{2}, \qquad (100)$$

Overall, from Eqs. (90) and (100),

$$\mathbf{y} = |\mathbf{H}\tilde{\mathbf{o}}_t|^2 - \mathbf{e}_t^{\text{couple}} + |\mathbf{H}\mathbf{e}_t^{\text{annea}}|^2 + \mathbf{n}^{\text{meas}}$$
. (101)

The non-linearity of Eq. (90) yields two terms in Eq. (101), that pose analytic challenges: a coupling term $\mathbf{e}_t^{\text{couple}}$; and a squared annealing error term $|\mathbf{H}\mathbf{e}_t^{\text{annea}}|^2$. We handle them by introducing a *relaxed* model

$$\mathbf{y} = |\mathbf{H}\tilde{\mathbf{o}}_t|^2 - \mathbf{e}_t^{\text{couple}} + |\mathbf{H}\mathbf{e}_t^{\text{annea}}|^2 + \tilde{\mathbf{n}}_t^{\text{meas}} - \sigma_t^2 \mathbf{z}_t \;. \tag{102}$$

We detail Eq. (102) and specifically $\mathbf{e}_t^{\mathrm{couple}}, \mathbf{e}_t^{\mathrm{annea}}, \tilde{\mathbf{n}}_t^{\mathrm{meas}}$ and \mathbf{z}_t in Appendix B.1.1 and Appendix B.1.2.

B.1.1 Relaxation of the Nonlinear Problem

Let

$$\Re(\mathbf{e}_{\tau}^{\mathrm{part}}), \Im(\mathbf{e}_{\tau}^{\mathrm{part}}) \sim N\left[0, \frac{1}{4}(\sigma_t^2 - \sigma_{t+1}^2)\mathbf{I}\right]$$
 (103)

be statistically independent Gaussian vectors. Recall that a sum of zero-mean Gaussian variables is a Gaussian, whose variance is the sum of the variances. Hence, in analogy to Eq. (64), and using Eq. (103)

$$\sum_{\tau=t_{1}}^{t_{2}} \Re(\mathbf{e}_{\tau}^{\text{part}}), \sum_{\tau=t_{1}}^{t_{2}} \Im(\mathbf{e}_{\tau}^{\text{part}}) \sim N\left[0, \frac{1}{4} \sum_{\tau=t_{1}}^{t_{2}} (\sigma_{\tau}^{2} - \sigma_{\tau+1}^{2}) \mathbf{I}\right] = N\left[0, \frac{1}{4} (\sigma_{t_{1}}^{2} - \sigma_{t_{2}}^{2}) \mathbf{I}\right].$$
(104)

Note that using Eq. (103)

$$\sum_{\tau=0}^{T} \Re(\mathbf{e}_{\tau}^{\text{part}}), \sum_{\tau=0}^{T} \Im(\mathbf{e}_{\tau}^{\text{part}}) \sim N\left(0, \frac{1}{4}\sigma_{0}^{2}\mathbf{I}\right) . \quad (105)$$

Define the random vectors

$$\mathbf{n}_{1}^{\text{part}} \equiv 2\Re(\mathbf{Ho}) \odot \sum_{\tau=0}^{T} \Re(\mathbf{e}_{\tau}^{\text{part}})$$

$$\sim 2\Re(\mathbf{Ho}) \odot N\left(0, \frac{1}{4}\sigma_{0}^{2}\mathbf{I}\right) = N\left(0, \sigma_{0}^{2} \left[\Re(\mathbf{Ho})\right]^{2}\right) ,$$
(106)

and

$$\mathbf{n}_{2}^{\text{part}} \equiv 2\Im(\mathbf{Ho}) \odot \sum_{\tau=0}^{T} \Im(\mathbf{e}_{\tau}^{\text{part}})$$

$$\sim 2\Im(\mathbf{Ho}) \odot N\left(0, \frac{1}{4}\sigma_{0}^{2}\mathbf{I}\right) = N\left(0, \sigma_{0}^{2} \left[\Im(\mathbf{Ho})\right]^{2}\right).$$
(107)

Recall that a sum of zero-mean Gaussian variables is a Gaussian, whose variance is the sum of the variances. So, from Eqs. (106) and (107), we obtain

$$\mathbf{n}_{1}^{\text{part}} + \mathbf{n}_{2}^{\text{part}} \sim N\left(0, \sigma_{0}^{2} \left[\Re(\mathbf{Ho})\right]^{2} + \sigma_{0}^{2} \left[\Im(\mathbf{Ho})\right]^{2}\right).$$
(108)

Using Eqs. (93,106,107), and (108), we can design dummy variables $\mathbf{e}_t^{\text{part}}$ such that,

$$\mathbf{n}^{\text{meas}} = \mathbf{n}_{1}^{\text{part}} + \mathbf{n}_{2}^{\text{part}}$$

$$= 2\Re(\mathbf{Ho}) \odot \sum_{\tau=0}^{T} \Re(\mathbf{e}_{\tau}^{\text{part}}) + 2\Im(\mathbf{Ho}) \odot \sum_{\tau=0}^{T} \Im(\mathbf{e}_{\tau}^{\text{part}}) . \tag{109}$$

Notice that Eq. (109) now has a form similar to the coupling term e_t^{couple} in Eq. (99).

Recall that we seek to derive $\nabla_{\tilde{\mathbf{o}}_t} \log p(\mathbf{y}|\tilde{\mathbf{o}}_t)$. This requires expressing \mathbf{y} in Eq. (101) using terms (besides $\tilde{\mathbf{o}}_t$) whose probability distributions are known and independent of $\tilde{\mathbf{o}}_t$. From Eq. (109), having an analytic expression of the probability distribution of \mathbf{n}^{meas} requires \mathbf{o} . In analogy to Eq. (71), we can hypothetically extract \mathbf{o} from Eq. (96). This leads to an expression of \mathbf{y} that contains statistically dependent terms, therefore, $\nabla_{\tilde{\mathbf{o}}_t} \log p(\mathbf{y}|\tilde{\mathbf{o}}_t)$ cannot be derived. Thus we make an approximation, assuming $\mathbf{o} \approx \tilde{\mathbf{o}}_t$ in Eq. (109). We do not yet use $\tilde{\mathbf{o}}_t$ as a denoised version. The approximation $\mathbf{o} \approx \tilde{\mathbf{o}}_t$ only handles \mathbf{n}^{meas} in Eq. (101), skewing it. Define approximate measurement noise

$$\tilde{\mathbf{n}}_{t}^{\text{meas}} = 2\Re(\mathbf{H}\tilde{\mathbf{o}}_{t}) \odot \sum_{\tau=0}^{T} \Re(\mathbf{e}_{\tau}^{\text{part}}) + 2\Im(\mathbf{H}\tilde{\mathbf{o}}_{t}) \odot \sum_{\tau=0}^{T} \Im(\mathbf{e}_{\tau}^{\text{part}}).$$
(110)

We continue to generalize the annealing error in Eq. (67) to a *complex-valued* annealing error: analogously to [16], we design $\mathbf{e}_t^{\mathrm{part}}$ such that

$$\mathbf{H}\mathbf{e}_{t}^{\text{annea}} = \sum_{\tau=t}^{T} \Re(\mathbf{e}_{\tau}^{\text{part}}) + j \sum_{\tau=t}^{T} \Im(\mathbf{e}_{\tau}^{\text{part}}) , \qquad (111)$$

where $j = \sqrt{-1}$. Insert $\mathbf{He}_t^{\text{annea}}$ from Eq. (111) into Eq. (99). This yields

$$\mathbf{e}_{t}^{\mathrm{couple}} =$$

$$2\Re(\mathbf{H}\tilde{\mathbf{o}}_t) \odot \sum_{\tau=t}^T \Re(\mathbf{e}_{\tau}^{\mathrm{part}}) + 2\Im(\mathbf{H}\tilde{\mathbf{o}}_t) \odot \sum_{\tau=t}^T \Im(\mathbf{e}_{\tau}^{\mathrm{part}}) .$$
(112)

Until here in this section, we detailed $\mathbf{e}_t^{\text{couple}}$, $\mathbf{e}_t^{\text{annea}}$, $\tilde{\mathbf{n}}_t^{\text{meas}}$ of Eq. (102). From this point, we detail \mathbf{z}_t that appears there.

B.1.2 The Term z_t

The vector \mathbf{z}_t is designed to address the challenge of the squared annealing error term $|\mathbf{H}\mathbf{e}_t^{\mathrm{annea}}|^2$. Inserting

Eq. (111) into Eq. (98), we obtain

$$|\mathbf{H}\mathbf{e}_{t}^{\text{annea}}|^{2} = [\Re(\mathbf{H}\mathbf{e}_{t}^{\text{annea}})]^{2} + [\Im(\mathbf{H}\mathbf{e}_{t}^{\text{annea}})]^{2}$$

$$= \left[\sum_{\tau=t}^{T} \Re(\mathbf{e}_{\tau}^{\text{part}})\right]^{2} + \left[\sum_{\tau=t}^{T} \Im(\mathbf{e}_{\tau}^{\text{part}})\right]^{2}. \tag{113}$$

A chi-squared distribution $\chi^2(\kappa)$ is defined by a sum of κ random variables: each independent, having a square-normal distribution [20]. Fig. 9 visualizes $\chi^2(\kappa)$. So, $|\mathbf{H}\mathbf{e}_t^{\mathrm{annea}}|^2$ in Eq. (113) is distributed $\chi^2(2)$, up to scale

$$f_{\chi^2(2)}\left(\frac{4}{\sigma_t^2}|\mathbf{H}\mathbf{e}_t^{\text{annea}}|^2\right) = \frac{1}{2}\exp\left(-\frac{4}{2\sigma_t^2}|\mathbf{H}\mathbf{e}_t^{\text{annea}}|^2\right),\tag{114}$$

where $f_{\chi^2(2)}$ operates element-wise. Analogously to Eq. (113), we propose two annealing error terms accordingly,⁷

$$\mathbf{z}_{t \to T} = \frac{\left[\sum_{\tau=t}^{T} \Re(\mathbf{e}_{\tau}^{\text{part}})\right]^{2}}{\sigma_{t}^{2}} + \frac{\left[\sum_{\tau=t}^{T} \Im(\mathbf{e}_{\tau}^{\text{part}})\right]^{2}}{\sigma_{t}^{2}}, \quad (115)$$

and

$$\mathbf{z}_{0 \to (t-1)} = \frac{\left[\sum_{\tau=0}^{t-1} \Re(\mathbf{e}_{\tau}^{\text{part}})\right]^2}{\sigma_t^2} + \frac{\left[\sum_{\tau=0}^{t-1} \Im(\mathbf{e}_{\tau}^{\text{part}})\right]^2}{\sigma_t^2} . \tag{116}$$

So, $\mathbf{z}_{0 \to (t-1)}, \mathbf{z}_{t \to T}$ in Eqs. (115) and (116) are each distributed $\chi^2(2)$, up to scale. Then using Eqs. (115) and (116), we define

$$\mathbf{z}_t = \mathbf{z}_{t \to T} - \mathbf{z}_{0 \to (t-1)} \ . \tag{117}$$

B.1.3 Concluding the Relaxed Model

Define

$$\mathbf{z}_t^{\text{remain}} \equiv |\mathbf{H}\mathbf{e}_t^{\text{annea}}|^2 - \sigma_t^2 \mathbf{z}_t \ .$$
 (118)

Using Eqs. (113,115,116,117), and (118),

$$\mathbf{z}_{t}^{\text{remain}} = \left[\sum_{\tau=0}^{t-1} \Re(\mathbf{e}_{\tau}^{\text{part}}) \right]^{2} + \left[\sum_{\tau=0}^{t-1} \Im(\mathbf{e}_{\tau}^{\text{part}}) \right]^{2}. \quad (119)$$

Using Eqs. (110) and (112), define

$$\mathbf{e}_{t}^{\text{remain}}(\tilde{\mathbf{o}}_{t}) \equiv \tilde{\mathbf{n}}_{t}^{\text{meas}} - \mathbf{e}_{t}^{\text{couple}}$$

$$= 2\Re(\mathbf{H}\tilde{\mathbf{o}}_{t}) \odot \sum_{\tau=0}^{t-1} \Re(\mathbf{e}_{\tau}^{\text{part}}) + 2\Im(\tilde{\mathbf{H}}\tilde{\mathbf{o}}_{t}) \odot \sum_{\tau=0}^{t-1} \Im(\mathbf{e}_{\tau}^{\text{part}}) . \tag{120}$$

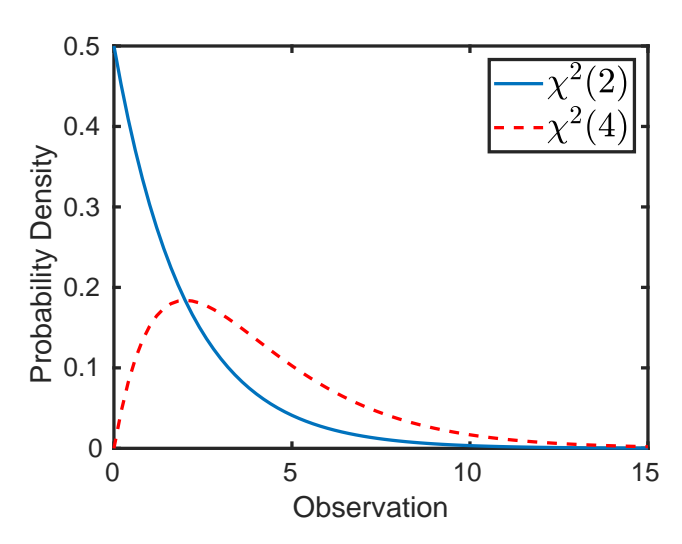


Figure 9. Visualization of the distribution $\chi^2(\kappa)$ for parameter values $\kappa=2,4$.

Inserting Eqs. (118) and (120) into the relaxed model in Eq. (102), yields

$$\mathbf{y} = |\mathbf{H}\tilde{\mathbf{o}}_{t}|^{2} + \tilde{\mathbf{n}}_{t}^{\text{meas}} - \mathbf{e}_{t}^{\text{couple}} + |\mathbf{H}\mathbf{e}_{t}^{\text{annea}}|^{2} - \sigma_{t}^{2}\mathbf{z}_{t}$$
$$= |\mathbf{H}\tilde{\mathbf{o}}_{t}|^{2} + \mathbf{e}_{t}^{\text{remain}}(\tilde{\mathbf{o}}_{t}) + \mathbf{z}_{t}^{\text{remain}}. \tag{121}$$

Using Eq. (121), $\nabla_{\tilde{\mathbf{o}}_t} \log p(\mathbf{y}|\tilde{\mathbf{o}}_t)$ can be derived analytically. To simplify notations, we define \mathbf{s} by

$$\Re(\mathbf{s}) \equiv \sum_{\tau=0}^{t-1} \Re(\mathbf{e}_{\tau}^{\text{part}}) , \ \Im(\mathbf{s}) \equiv \sum_{\tau=0}^{t-1} \Im(\mathbf{e}_{\tau}^{\text{part}}) . \tag{122}$$

Inserting Eq. (122) in Eq. (120), yields

$$\mathbf{e}_{t}^{\text{remain}}(\tilde{\mathbf{o}}_{t}) = 2\Re(\tilde{\mathbf{o}}_{t}) \odot \Re(\mathbf{s}) + 2\Im(\tilde{\mathbf{o}}_{t}) \odot \Im(\mathbf{s})$$
. (123)

Inserting Eq. (122) in Eq. (119), yields

$$\mathbf{z}_t^{\text{remain}} = [\Re(\mathbf{s})]^2 + [\Im(\mathbf{s})]^2. \tag{124}$$

Then, using $\mathbf{e}_t^{\text{remain}}, \mathbf{z}_t^{\text{remain}}$ from Eqs. (123) and (124) in Eq. (121),

$$\mathbf{y} = |\mathbf{H}\tilde{\mathbf{o}}_{t}|^{2} + 2\Re(\mathbf{H}\tilde{\mathbf{o}}_{t}) \odot \Re(\mathbf{s}) + 2\Im(\mathbf{H}\tilde{\mathbf{o}}_{t}) \odot \Im(\mathbf{s}) + ([\Re(\mathbf{s})]^{2} + [\Im(\mathbf{s})]^{2})$$
$$= [\Re(\mathbf{H}\tilde{\mathbf{o}}_{t}) + \Re(\mathbf{s})]^{2} + [\Im(\mathbf{H}\tilde{\mathbf{o}}_{t}) + \Im(\mathbf{s})]^{2} . \tag{125}$$

B.1.4 Gradient of the Relaxed Model

Using Eq. (125), we can derive $p(\mathbf{y}|\tilde{\mathbf{o}}_t)$ analytically. Let I_0, I_1 be the modified Bessel functions of the first kind [5], which operate element-wise. Let $\sqrt{\cdot}$ and $\exp(\cdot)$ operate element-wise. Let $(\cdot)^{\top}$ denote transposition. Let $\prod[\cdot]$ be

⁷Note that $\sigma_t^2 z_t$ in Eq. (102) can be considered as an additional annealing error in the measurement domain.

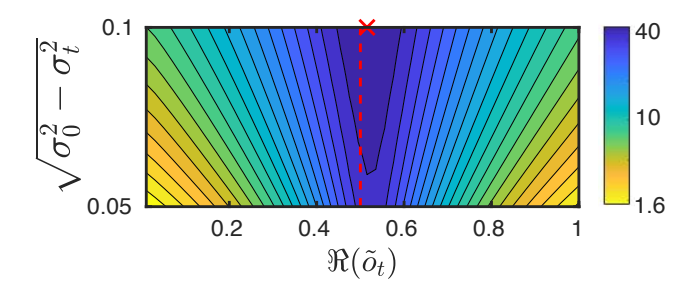


Figure 10. A visualization of Eq. (129), that is, the log-likelihood of Eq. (121). Here $\mathbf{H}=1$ and o=0.5+0.5j. We present $\Re(o)$ by a red dashed line. Here, y is obtained by Eq. (90), using $\sigma_0=0.1$. The red cross mark depicts the log-likelihood maximum.

an operator that outputs the element-wise product of a given vector, that is, for column vector $\mathbf{v} = [v_1, v_2, \dots, v_{q^{\text{meas}}}]^{\top}$,

$$\prod[\mathbf{v}] = v_1 v_2 \dots v_{q^{\text{meas}}} . \tag{126}$$

From Sec. 2.3, recall vectors $\tilde{\mathbf{o}}_t \in \mathbb{C}^q$ and $\mathbf{y} \in \mathbb{R}^{q^{\mathrm{meas}}}$, and the linear transformation matrix $\mathbf{H} \in \mathbb{C}^{q^{\mathrm{meas}} \times q}$. Let 1 be a column vector of length q^{meas} , all of whose elements have value 1.

The probability distribution function of $\left[\Re(\mathbf{H}\tilde{\mathbf{o}}_t)+\Re(\mathbf{s})\right]^2+\left[\Im(\mathbf{H}\tilde{\mathbf{o}}_t)+\Im(\mathbf{s})\right]^2$ in Eq. (125) is non-central chi-squared of the second kind [20], up to a scaling by $(\sigma_0^2-\sigma_t^2)$. Thus,

$$p(\mathbf{y}|\tilde{\mathbf{o}}_t) = \prod \left[\frac{1}{2(\sigma_0^2 - \sigma_t^2)} \exp\left(-\frac{\mathbf{y} + |\mathbf{H}\tilde{\mathbf{o}}_t|^2}{2(\sigma_0^2 - \sigma_t^2)}\right) \\ \odot I_0\left(\frac{|\mathbf{H}\tilde{\mathbf{o}}_t| \odot \sqrt{\mathbf{y}}}{\sigma_0^2 - \sigma_t^2}\right) \right] . \quad (127)$$

The right-hand term in Eq. (127) can be written

$$p(\mathbf{y}|\tilde{\mathbf{o}}_{t}) = \frac{1}{[2(\sigma_{0}^{2} - \sigma_{t}^{2})]^{q^{\text{meas}}}} \exp\left(-\frac{\mathbf{1}^{\top} \left[\mathbf{y} + |\mathbf{H}\tilde{\mathbf{o}}_{t}|^{2}\right]}{2(\sigma_{0}^{2} - \sigma_{t}^{2})}\right)$$
$$\prod \left[I_{0}\left(\frac{|\mathbf{H}\tilde{\mathbf{o}}_{t}| \odot \sqrt{\mathbf{y}}}{\sigma_{0}^{2} - \sigma_{t}^{2}}\right)\right]. \tag{128}$$

Take the \log value element-wise on both sides of Eq. (128). This results in

$$\log p(\mathbf{y}|\tilde{\mathbf{o}}_t) = Q - \frac{\mathbf{1}^{\top} \left[\mathbf{y} + |\mathbf{H}\tilde{\mathbf{o}}_t|^2 \right]}{2(\sigma_0^2 - \sigma_t^2)} + \mathbf{1}^{\top} \left[\log I_0 \left(\frac{|\mathbf{H}\tilde{\mathbf{o}}_t| \odot \sqrt{\mathbf{y}}}{\sigma_0^2 - \sigma_t^2} \right) \right], (129)$$

where $Q=-q^{\rm meas}\log[2(\sigma_0^2-\sigma_t^2)]$. We visualize $\log p(\mathbf{y}|\tilde{\mathbf{o}}_t)$ in Fig. 10.

The terms Q and \mathbf{y} in Eq. (129) are independent of $\tilde{\mathbf{o}}_t$. Therefore, $\nabla_{\tilde{\mathbf{o}}_t} Q = 0$ and $\nabla_{\tilde{\mathbf{o}}_t} \mathbf{y} = 0$. Moreover, note that holds

$$\mathbf{1}^{\top} \left[|\mathbf{H} \tilde{\mathbf{o}}_t|^2 \right] = [\mathbf{H} \tilde{\mathbf{o}}_t]^{\top} [\mathbf{H} \tilde{\mathbf{o}}_t] . \tag{130}$$

Define $\bar{\mathbf{H}}^{\top}$ as the conjugate transpose of \mathbf{H} . Then,

$$\nabla_{\tilde{\mathbf{o}}_{t}} \left(Q + \frac{\mathbf{1}^{\top} \left[\mathbf{y} + |\mathbf{H}\tilde{\mathbf{o}}_{t}|^{2} \right]}{2(\sigma_{0}^{2} - \sigma_{t}^{2})} \right) = \nabla_{\tilde{\mathbf{o}}_{t}} \left(\frac{\mathbf{1}^{\top} \left[|\mathbf{H}\tilde{\mathbf{o}}_{t}|^{2} \right]}{2(\sigma_{0}^{2} - \sigma_{t}^{2})} \right)$$

$$= \nabla_{\tilde{\mathbf{o}}_{t}} \left(\frac{\left[\mathbf{H}\tilde{\mathbf{o}}_{t} \right]^{\top} \left[\mathbf{H}\tilde{\mathbf{o}}_{t} \right]}{2(\sigma_{0}^{2} - \sigma_{t}^{2})} \right) = \bar{\mathbf{H}}^{\top} \frac{\mathbf{H}\tilde{\mathbf{o}}_{t}}{\sigma_{0}^{2} - \sigma_{t}^{2}}. \tag{131}$$

By definition, the modified Bessel function of the first kind holds [5],

$$\nabla_{\mathbf{v}} I_0(\mathbf{v}) = I_1(\mathbf{v}), \ \forall \mathbf{v} \ , \tag{132}$$

per element. Therefore,

$$\nabla_{\mathbf{v}}[\log I_0(\mathbf{v})] = I_1(\mathbf{v})/I_0(\mathbf{v}) , \qquad (133)$$

where division is performed element-wise. Let

$$\mathcal{L}(\mathbf{v}) \equiv \mathbf{1}^{\top} [\log I_0(\mathbf{v})] = \log I_0(v_1) + \dots + \log I_0(v_{q^{\text{meas}}}).$$
(134)

Define vectors

$$\boldsymbol{\omega}(\tilde{\mathbf{o}}_t) = \mathbf{H}\tilde{\mathbf{o}}_t \in \mathbb{C}^{q^{\text{meas}}}, \tag{135}$$

and

$$\mathbf{h}[\boldsymbol{\omega}(\tilde{\mathbf{o}}_t), \mathbf{y}] = \frac{|\boldsymbol{\omega}(\tilde{\mathbf{o}}_t)| \odot \sqrt{\mathbf{y}}}{\sigma_0^2 - \sigma_t^2} \in \mathbb{R}^{q^{\text{meas}}}.$$
 (136)

From Eqs. (134) to (136)

$$\mathbf{1}^{\top} \left[\log I_0 \left(\frac{|\mathbf{H} \tilde{\mathbf{o}}_t| \odot \sqrt{\mathbf{y}}}{\sigma_0^2 - \sigma_t^2} \right) \right] = \mathcal{L}(\mathbf{h}[\boldsymbol{\omega}(\tilde{\mathbf{o}}_t), \mathbf{y}]) \in \mathbb{R} .$$
(137)

A gradient of a scalar is a vector, thus, $\nabla_{\mathbf{h}} \mathcal{L} \in \mathbb{R}^{q^{\mathrm{meas}}}$ and

$$\nabla_{\tilde{\mathbf{o}}_t} \left(\mathbf{1}^{\top} \left[\log I_0 \left(\frac{|\mathbf{H} \tilde{\mathbf{o}}_t| \odot \sqrt{\mathbf{y}}}{\sigma_0^2 - \sigma_t^2} \right) \right] \right) = \nabla_{\tilde{\mathbf{o}}_t} \mathcal{L} \in \mathbb{C}^q .$$
(138)

A gradient of a *vector* is a *matrix*. Specifically, from Eqs. (135) and (136), $[\nabla_{\tilde{\mathbf{o}}_t}\boldsymbol{\omega}] \in \mathbb{C}^{q \times q^{\mathrm{meas}}}$ and $[\nabla_{\boldsymbol{\omega}}\mathbf{h}] \in \mathbb{C}^{q^{\mathrm{meas}} \times q^{\mathrm{meas}}}$. Using the chain rule

$$\nabla_{\tilde{\mathbf{o}}_{t}} \mathcal{L}(\mathbf{h}[\boldsymbol{\omega}(\tilde{\mathbf{o}}_{t}), \mathbf{y}]) = [\nabla_{\tilde{\mathbf{o}}_{t}} \boldsymbol{\omega}] [\nabla_{\boldsymbol{\omega}} \mathbf{h}] \nabla_{\mathbf{h}} \mathcal{L} . \tag{139}$$

Hence, we need to compute the partial derivatives that appear in the right-hand side of Eq. (139).

Note that $\forall \nu \in [1, q^{\text{meas}}],$

$$\frac{\partial}{\partial v_{\nu}} \mathcal{L} = \frac{\partial}{\partial v_{\nu}} \log I_0(v_{\nu}) = I_1(v_{\nu}) / I_0(v_{\nu}) . \tag{140}$$

Therefore,

$$\nabla_{\mathbf{v}} \mathcal{L}(\mathbf{v}) = I_1(\mathbf{v}) / I_0(\mathbf{v}) \in \mathbb{R}^{q^{\text{meas}}}. \tag{141}$$

Define

$$\mathcal{I}(\tilde{\mathbf{o}}_t, \mathbf{y}) = I_1(\mathbf{h}[\boldsymbol{\omega}(\tilde{\mathbf{o}}_t), \mathbf{y}]) / I_0(\mathbf{h}[\boldsymbol{\omega}(\tilde{\mathbf{o}}_t), \mathbf{y}]) , \quad (142)$$

where division is performed element-wise. Fig. 11 visualizes \mathcal{I} as defined in Eq. (142). Using Eqs. (141) and (142),

$$\nabla_{\mathbf{h}} \mathcal{L}(\mathbf{h}) = \mathcal{I}(\tilde{\mathbf{o}}_t, \mathbf{y}) \in \mathbb{R}^{q^{\text{meas}}}$$
 (143)

A definition for a complex-valued derivative of elementwise modulus is [18]

$$\frac{\partial}{\partial v_{\nu}}|v_{\nu}| = v_{\nu}/|v_{\nu}|, \ \forall \nu \in [1, q^{\text{meas}}] \ . \tag{144}$$

Based on a vector \mathbf{v} , define a diagonal matrix by $\mathbf{D} = \mathrm{diag}\{\mathbf{v}\}$ such that the diagonal $\mathbf{D}_{\nu,\nu} = v_{\nu}$, and off-diagonal elements of \mathbf{D} are null. Using Eq. (144)

$$\nabla_{\mathbf{v}}|\mathbf{v}| = \operatorname{diag}\{\mathbf{v}/|\mathbf{v}|\} \in \mathbb{C}^{q^{\operatorname{meas}} \times q^{\operatorname{meas}}}$$
. (145)

Thus, using Eqs. (136) and (145)

$$[\nabla_{\boldsymbol{\omega}} \mathbf{h}(\boldsymbol{\omega}, \mathbf{y})] = \operatorname{diag} \left\{ \frac{\sqrt{\mathbf{y}}}{\sigma_0^2 - \sigma_t^2} \odot \frac{\boldsymbol{\omega}}{|\boldsymbol{\omega}|} \right\}.$$
 (146)

From Eq. (135), the gradient of the *vector* ω results in a matrix

$$[\nabla_{\tilde{\mathbf{o}}_t} \boldsymbol{\omega}] = \bar{\mathbf{H}}^\top . \tag{147}$$

Using Eqs. (143), (146) and (147),

 $\left[\nabla_{\tilde{\mathbf{o}}_t}\omega\right]\left[\nabla_{\boldsymbol{\omega}}\mathbf{h}\right]\nabla_{\mathbf{h}}\mathcal{L}$

$$= \bar{\mathbf{H}}^{\top} \operatorname{diag} \left\{ \frac{\sqrt{\mathbf{y}}}{\sigma_0^2 - \sigma_t^2} \odot \frac{\mathbf{H} \tilde{\mathbf{o}}_t}{|\mathbf{H} \tilde{\mathbf{o}}_t|} \right\} \mathcal{I}(\tilde{\mathbf{o}}_t, \mathbf{y}) . \quad (148)$$

By definition, pairs of vectors $\mathbf{v_1}, \mathbf{v_2}$ having the same length satisfy $\mathrm{diag}\{\mathbf{v_1}\}\mathbf{v_2} = \mathbf{v_1} \odot \mathbf{v_2}$. Thus, Eq. (148) can be written in a more compact way

$$\left[\nabla_{\tilde{\mathbf{o}}_t}\boldsymbol{\omega}\right]\left[\nabla_{\boldsymbol{\omega}}\mathbf{h}\right]\nabla_{\mathbf{h}}\mathcal{L}$$

$$= \mathbf{\bar{H}}^{\top} \left[\frac{\sqrt{\mathbf{y}}}{\sigma_0^2 - \sigma_t^2} \odot \frac{\mathbf{H} \tilde{\mathbf{o}}_t}{|\mathbf{H} \tilde{\mathbf{o}}_t|} \odot \mathcal{I}(\tilde{\mathbf{o}}_t, \mathbf{y}) \right] . \quad (149)$$

Using Eqs. (137), (139) and (149),

$$\nabla_{\tilde{\mathbf{o}}_{t}} \underbrace{\mathbf{1}^{\top} \left[\log I_{0} \left(\frac{|\mathbf{H}\tilde{\mathbf{o}}_{t}| \odot \sqrt{\mathbf{y}}}{\sigma_{0}^{2} - \sigma_{t}^{2}} \right) \right]}_{\mathcal{L}(\mathbf{h}|\omega)} = \left[\nabla_{\tilde{\mathbf{o}}_{t}} \omega \right] \left[\nabla_{\omega} \mathbf{h} \right] \nabla_{\mathbf{h}} \mathcal{L}$$

$$= \bar{\mathbf{H}}^{\top} \left[\frac{\mathbf{H}\tilde{\mathbf{o}}_{t}}{\sigma_{0}^{2} - \sigma_{t}^{2}} \odot \mathcal{I}(\tilde{\mathbf{o}}_{t}, \mathbf{y}) \odot \frac{\sqrt{\mathbf{y}}}{|\mathbf{H}\tilde{\mathbf{o}}_{t}|} \right]. \tag{150}$$

Overall, using Eqs. (129), (131) and (150), the complexvalued derivative of $\log p(\mathbf{y}|\tilde{\mathbf{o}}_t)$ is

 $\nabla_{\tilde{\mathbf{o}}_t} \log p(\mathbf{y}|\tilde{\mathbf{o}}_t) =$

$$\bar{\mathbf{H}}^{\top} \left(\frac{\mathbf{H}\tilde{\mathbf{o}}_t}{\sigma_0^2 - \sigma_t^2} \odot \left[\mathcal{I}(\tilde{\mathbf{o}}_t, \mathbf{y}) \odot \frac{\sqrt{\mathbf{y}}}{|\mathbf{H}\tilde{\mathbf{o}}_t|} - 1 \right] \right) . \tag{151}$$

B.2. Gradient of the Prior: Complex-Valued Objects

We need to derive $\nabla_{\tilde{\mathbf{o}}_t} \log p(\tilde{\mathbf{o}}_t)$ in Eq. (95) for annealed Langevin dynamics of complex-valued objects. Analogously to Appendix A.2, before imaging takes place, we pre-train a DNN $h_{\Theta}^{\text{Complex}}$ to approximate $\nabla_{\tilde{\mathbf{o}}_t} \log p(\tilde{\mathbf{o}}_t)$. This process is described in this section. Moreover, from Eq. (96), $\tilde{\mathbf{o}}_t$ is assumed to be a noisy version of the sought object o. Thus, $h_{\Theta}^{\text{Complex}}$ acts as a denoiser for complex-valued objects.

In analogy to Eq. (96), let (o, o') be a synthetic pair of clean and noisy complex-valued objects, rendered using

$$\mathbf{o}' = \mathbf{o} + \mathbf{n}^{\text{train}} \,. \tag{152}$$

Here $\Re(\mathbf{n}^{\text{train}})$, $\Im(\mathbf{n}^{\text{train}}) \sim N(0, \sigma^2 \mathbf{I})$, where σ is an arbitrary noise level. Using Eq. (152),

$$p(\mathbf{o}'|\mathbf{o}) = p(\mathbf{o}' - \mathbf{o}|\mathbf{o}) = p(\mathbf{n}^{\text{train}}|\mathbf{o})$$
$$= \frac{1}{\sqrt{2\pi\sigma^2}} \exp\left[-\frac{|\mathbf{o}' - \mathbf{o}|^2}{2\sigma^2}\right] . \quad (153)$$

By definition, the marginal distribution $p(\mathbf{o}')$ can be written as

$$p(\mathbf{o}') = \int p(\mathbf{o}'|\mathbf{o})p(\mathbf{o})d\mathbf{o}$$
 (154)

Insert Eq. (153) into Eq. (154). This yields

$$p(\mathbf{o}') = \int \frac{1}{\sqrt{2\pi\sigma^2}} \exp\left[-\frac{|\mathbf{o}' - \mathbf{o}|^2}{2\sigma^2}\right] p(\mathbf{o}) d\mathbf{o}$$
. (155)

Then, the gradient of Eq. (155) satisfies

$$\nabla_{\mathbf{o}'} p(\mathbf{o}') = \int \frac{1}{\sqrt{2\pi\sigma^2}} \nabla_{\mathbf{o}'} \exp\left[-\frac{|\mathbf{o}' - \mathbf{o}|^2}{2\sigma^2}\right] p(\mathbf{o}) d\mathbf{o}$$
$$= \int \left[\frac{\mathbf{o} - \mathbf{o}'}{\sigma^2}\right] \frac{1}{\sqrt{2\pi\sigma^2}} \exp\left[-\frac{|\mathbf{o}' - \mathbf{o}|^2}{2\sigma^2}\right] p(\mathbf{o}) d\mathbf{o} . \tag{156}$$

Insert the definition of $p(\mathbf{o}'|\mathbf{o})$ given in Eq. (153) to Eq. (156). This results in

$$\nabla_{\mathbf{o}'} p(\mathbf{o}') = \int \left[\frac{\mathbf{o} - \mathbf{o}'}{\sigma^2} \right] p(\mathbf{o}'|\mathbf{o}) p(\mathbf{o}) d\mathbf{o} . \tag{157}$$

Divide both sides of Eq. (157) by p(o'). This leads to

$$\frac{\nabla_{\mathbf{o}'} p(\mathbf{o}')}{p(\mathbf{o}')} = \int \left[\frac{\mathbf{o} - \mathbf{o}'}{\sigma^2} \right] \frac{p(\mathbf{o}'|\mathbf{o}) p(\mathbf{o})}{p(\mathbf{o}')} d\mathbf{o} . \tag{158}$$

Recall Bayes rule.

$$p(\mathbf{o}|\mathbf{o}') = \frac{p(\mathbf{o}'|\mathbf{o})p(\mathbf{o})}{p(\mathbf{o}')}.$$
 (159)

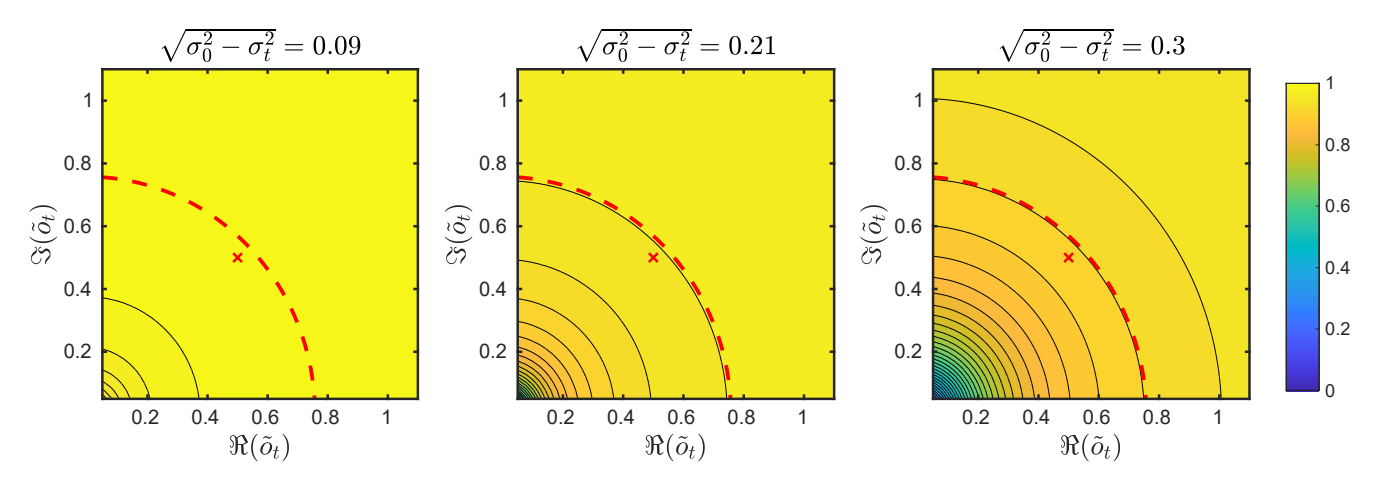


Figure 11. A visualization of $\mathcal{I}(\tilde{o}_t, \mathbf{y})$ in Eq. (142) for different values of σ_t . Here $\mathbf{H} = 1$ and o = 0.5 + 0.5j, while y is obtained by Eq. (90) using $\sigma_0 = 0.3$. We present \sqrt{y} by a red dashed line. The red cross marks o.

Insert Eq. (159) into Eq. (158). This results in

$$\frac{\nabla_{\mathbf{o}'}p(\mathbf{o}')}{p(\mathbf{o}')} = \int \left[\frac{\mathbf{o} - \mathbf{o}'}{\sigma^2}\right] p(\mathbf{o}|\mathbf{o}') d\mathbf{o} . \tag{160}$$

The left-hand side of Eq. (160) satisfies

$$\frac{\nabla_{\mathbf{o}'} p(\mathbf{o}')}{p(\mathbf{o}')} = \nabla_{\mathbf{o}'} \log p(\mathbf{o}') . \tag{161}$$

The right-hand side of Eq. (160) can be written as

$$\int \left[\frac{\mathbf{o} - \mathbf{o}'}{\sigma^2} \right] p(\mathbf{o}|\mathbf{o}') d\mathbf{o} = \mathbb{E} \left[\frac{\mathbf{o} - \mathbf{o}'}{\sigma^2} \middle| \mathbf{o}' \right] . \tag{162}$$

Overall, from Eqs. (160) to (162)

$$\nabla_{\mathbf{o}'} \log p(\mathbf{o}') = \mathbb{E} \left[\frac{\mathbf{o} - \mathbf{o}'}{\sigma^2} \middle| \mathbf{o}' \right] . \tag{163}$$

The expectation in Eq. (163) cannot be calculated analytically. The reason is that the probability distribution of o is not accessible. Therefore, we approximate the expectation in Eq. (163) using a DNN. We generate a large dataset of synthetic pairs of clean and noisy objects $(\mathbf{o}, \mathbf{o}')$ using Eq. (152), with various standard deviations σ . Then, we train a deep neural network $h_{\Theta}^{\mathrm{Complex}}(\mathbf{o}'|\sigma)$, such that

$$\hat{\Theta} = \arg\min_{\Theta} \mathbb{E} \left[\left\| \frac{\mathbf{o} - \mathbf{o}'}{\sigma^2} - h_{\Theta}^{\text{complex}}(\mathbf{o}'|\sigma) \right\|_2^2 \right] . \quad (164)$$

Here, the expectation \mathbb{E} is approximated as an empirical average of all pairs in the training set of clean and noisy complex-valued objects (o, o'). Overall, using Eqs. (95), (151), (163) and (164)

 $\nabla_{\tilde{\mathbf{o}}_t} \log p(\tilde{\mathbf{o}}_t | \mathbf{y}) =$

$$\frac{\tilde{\mathbf{o}}_{t}}{2(\sigma_{0}^{2} - \sigma_{t}^{2})} \odot \left[\mathcal{I}(\tilde{\mathbf{o}}_{t}, \mathbf{y}) \odot \frac{\sqrt{\mathbf{y}}}{|\tilde{\mathbf{o}}_{t}|} - 1 \right] + h_{\hat{\Theta}}^{\text{complex}}(\tilde{\mathbf{x}}_{t} | \sigma_{t}) . \tag{165}$$

C. Fourier Ptychography: Additional Background

Here we describe a Fourier ptychography imaging system that was used in experiments that are detailed in [41]. Let ${\bf r}$ represent a 2D spatial coordinate. Let ${\bf \lambda}$ be the wavelength. The system has an array of M LEDs. Let ${\bf \delta}_m$ be the illumination angle created by the mth LED. The model is that a LED creates illumination by a plane wave $u_m^{\rm LED}({\bf r})$. The plane wave angle ${\bf \delta}_m$ corresponds to a spatial frequency

$$\mathbf{k}_m = \sin(\boldsymbol{\delta}_m)/\lambda \;, \tag{166}$$

that is,

$$u_m^{\text{LED}}(\mathbf{r}) = \exp\left(j\mathbf{k}_m \cdot \mathbf{r}\right).$$
 (167)

Let $o(\mathbf{r})$ be the transmittance of an optically-thin object. The wave exiting the object is a multiplication of this transmittance and $u_m^{\mathrm{LED}}(\mathbf{r})$ of Eq. (167):

$$u_m^{\text{obj}}(\mathbf{r}) = o(\mathbf{r}) \exp(j\mathbf{k}_m \cdot \mathbf{r})$$
 (168)

Let $\mathcal{F},\mathcal{F}^{-1}$ denote the spatial Fourier transform and its inverse, respectively. Define

$$O(\mathbf{k}) = \mathcal{F}[o](\mathbf{k}) . \tag{169}$$

At the pupil plane (see Fig. 1), the light field corresponds to the spatial Fourier transform of $u_m^{\text{obj}}(\mathbf{r})$ in Eq. (168),

$$U_m^{\text{obj}}(\mathbf{k}) = \mathcal{F}[u_m^{\text{obj}}](\mathbf{k}) = O(\mathbf{k} - \mathbf{k}_m) .$$
 (170)

Let $P(\mathbf{k})$ be a low-pass filter, that is, a binary circle centered at the frequency origin. Denote by k^{NA} the radius of $P(\mathbf{k})$, determined by the system numerical aperture (NA) and λ . Let $\mathcal{M}(\cdot)$ be a magnification operator of an imaging system. The light intensity at the image plane resulting from a single LED is

$$y_m(\mathbf{r}) = \mathcal{N}\left(\mathcal{M}[|\mathcal{F}^{-1}[P(\mathbf{k})O(\mathbf{k} - \mathbf{k}_m)]|^2]\right)(\mathbf{r})$$
. (171)

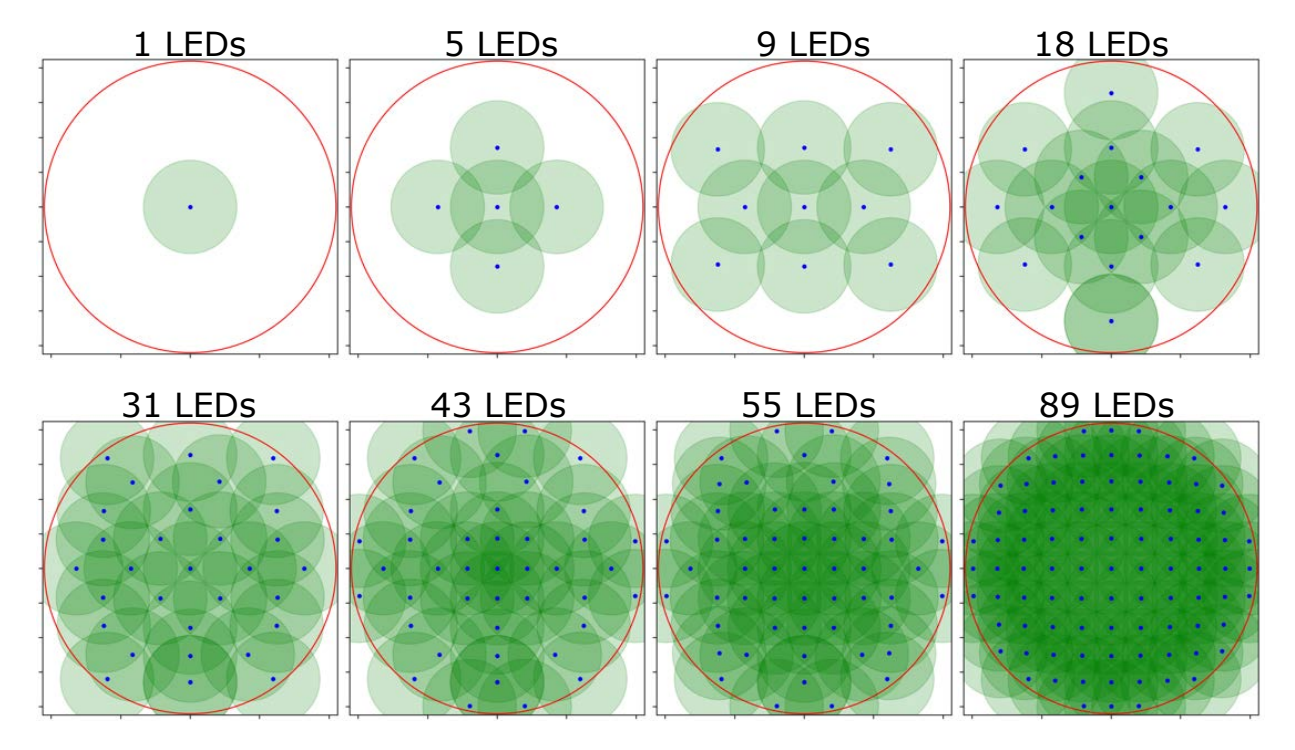


Figure 12. Visualization of coverage of the object's Fourier domain. The red circle is determined by the maximal LED angle of the system, having a frequency radius of k^{max} . The blue dots correspond to \mathbf{k}_m of the LEDs, while the half-transparent green circles are the measured spectra domains around each \mathbf{k}_m , having frequency radius of k^{NA} .

Hence, the angles of the LEDs and the support of $P(\mathbf{k})$ define the measured frequency content of the object. Fig. 12 visualizes the measured frequency content of the object for different numbers of LEDs.

D. Additional Results

In this section, we present additional results that were not included in Sec. 4, for space limitations. Furthermore, we detail and elaborate the experimental results presented in Sec. 4.

D.1. Denoising Poissonian Image Intensities

Here we show additional examples for Poisson denoising. The experimental details are provided in Sec. 4.1. Define the recovery of an MMSE estimator for Poisson denoising, corresponding to noise level σ_0 , as

$$\hat{\mathbf{x}}^{\text{MMSE}} = \mathbf{y} - h_{\Theta}^{\text{Poisson}}(\mathbf{y}|\sigma_0)$$
. (172)

Figs. 13 to 16 compare our results, for different noise levels σ_0 , with Eq. (172). Our denoised images have higher quality than the MMSE solution, which is blurred.

D.2. Phase Retrieval

As described in Sec. 4.2, phase retrieval can be modeled using $\mathbf{H} = \mathbf{F}$, that is,

$$\mathbf{y} = \mathcal{N}(|\mathbf{Fo}|^2) \ . \tag{173}$$

Method	PSNR
HIO [9]	17.9
BM3D-prGAMP [25]	21.0
BM3D-ADMM [24]	21.8
DnCNN-ADMM [24]	22.0
prDeep [24]	26.4
Ours	28.9

Table 2. PSNR (Eq. 52) for the "natural" images data set suggested in [24], using noise level $\sigma_0 = 4/255$.

Here \mathcal{N} contains photon noise and quantization, the latter using 8 bits per pixel. Moreover, in our demonstration, \mathbf{o} is a real-valued image. Note that even so, the measurement \mathbf{y} lacks phase information.

We compare our method (Algorithm 3) for phase retrieval, vs. prior art. We follow the experiment suggested in [24]. First, we trained $h_{\Theta}^{\text{Complex}}(o'|\sigma)$ (Eq. 164) with overlapping patches drawn from 400 images in the Berkeley Segmentation Dataset [23]. Then, we evaluate our method on a test set of 6 "natural" images, presented in Fig. 17. We simulate for each image from the test set its noisy intensity measurements using Eq. (173) with noise level $\sigma_0 = 4/255$, as described in Sec. 2.2.

As reported in [24], the results were sensitive to initialization. So, as done in [24], we initialized our method us-

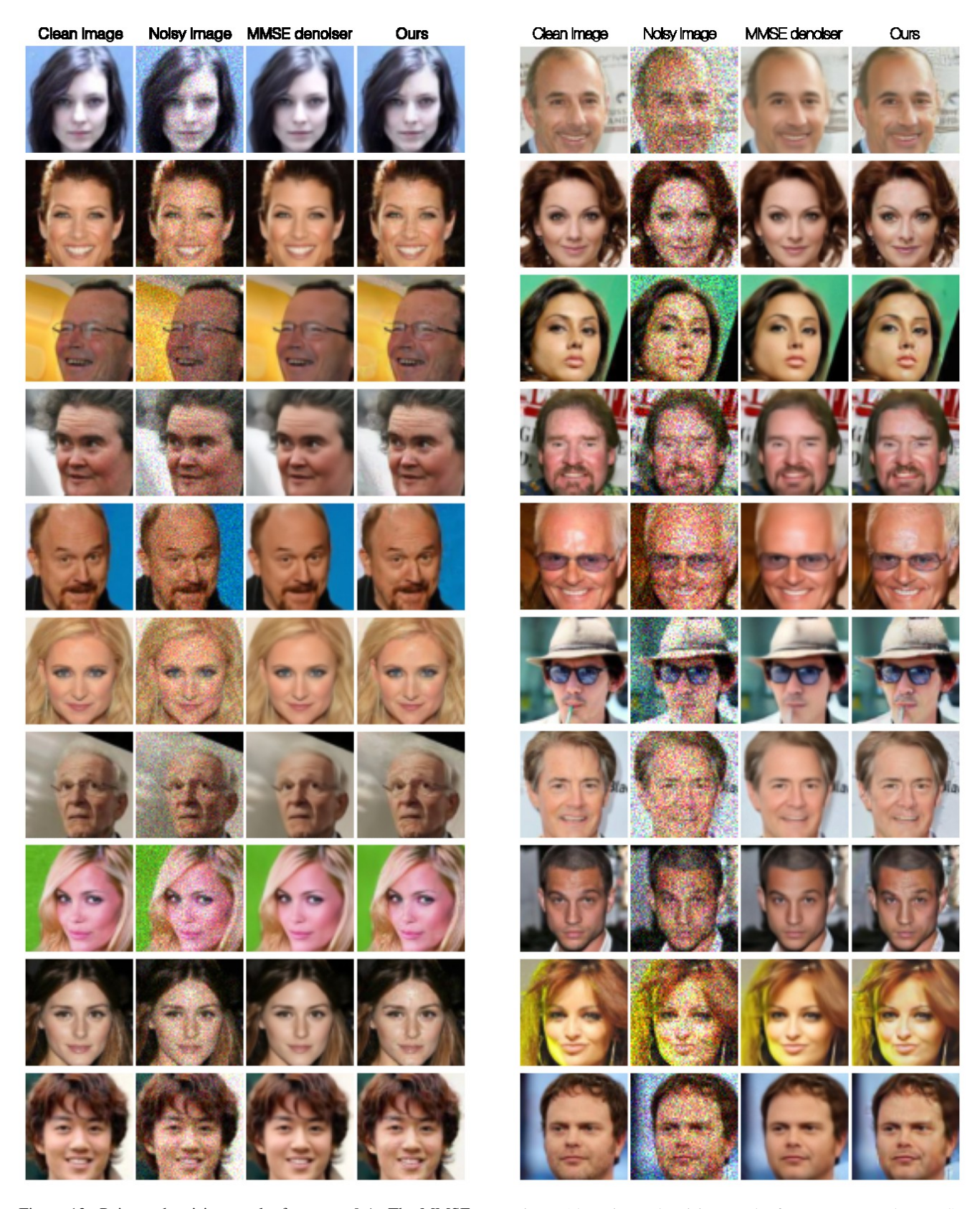


Figure 13. Poisson denoising results for $\sigma_0=0.1$. The MMSE denoised results have blur.

Figure 14. Poisson denoising results for $\sigma_0=0.2$. The MMSE denoised results have blur.



Figure 15. Poisson denoising results for $\sigma_0=0.3.$ The MMSE denoised results have blur.

Figure 16. Poisson denoising results for $\sigma_0=0.4$. The MMSE denoised results have blur.



Figure 17. Qualitative comparison between the ground-truth images in the dataset suggested by [24] and our recovery.

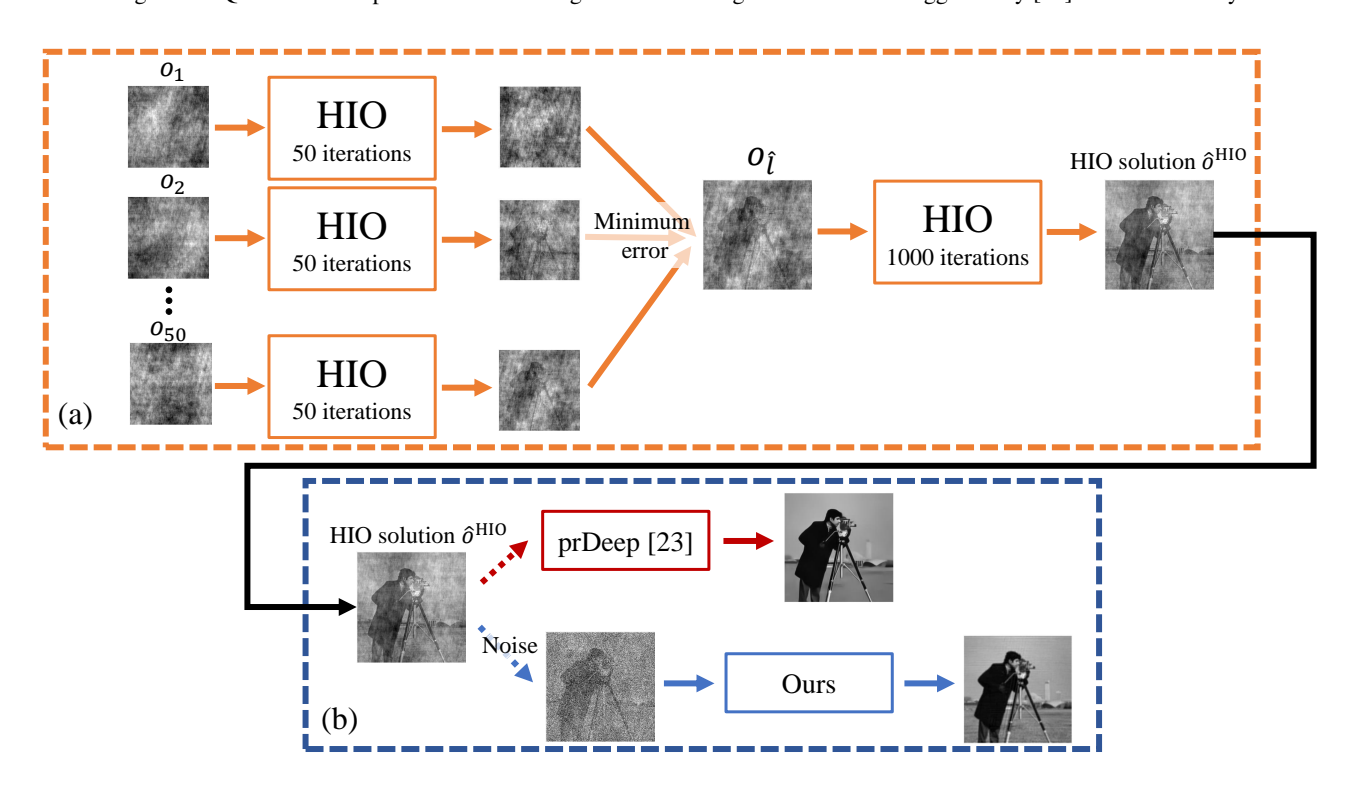


Figure 18. A block diagram of the phase retrieval experiment. (a) Initialization using the HIO [9] algorithm. (b) Final recovery using prDeep [24] and our method (Algorithm 3). The process of (a) and (b) is repeated three times, resulting in three solutions for each method $\{\hat{\mathbf{o}}_{\ell}^{\text{ours}}\}_{\ell=1}^3$, $\{\hat{\mathbf{o}}_{\ell}^{\text{prDeep}}\}_{\ell=1}^3$. Then, for each method, the reconstruction with the smallest error in Eq. (175) (out of the three) is used as its final estimation.

ing a process relying on the Hybrid Input-Output (HIO) [9] algorithm. Fig. 18 presents a block diagram of the process. Let ψ be a random Gaussian vector. We initialized 50 possible candidate solutions $\{\mathbf{o}_l\}_{l=1}^{50}$ such that $\mathbf{F}\mathbf{o}_l = \sqrt{\mathbf{y}}\exp(j2\pi\psi_l)$. As is [24], we ran the HIO algorithm for 50 iterations, for each of these candidates. The recon-

structed candidate is the candidate with the lowest error

$$\hat{l} = \arg\min_{l} \left\| \mathbf{y} - |\mathbf{Fo}_{l}|_{2}^{2} \right\|_{2}^{2} . \tag{174}$$

Then, we initialize the HIO algorithm using $o_{\hat{l}}$, and ran the HIO algorithm for 1000 iterations again, resulting in the

HIO result $\hat{\mathbf{o}}^{\mathrm{HIO}}$. We initialize our method in Algorithm 3 with a noisy version of the HIO result. Following [24], this process was repeated three times $\ell = \{1, 2, 3\}$, and the reconstruction $\hat{\mathbf{o}}_{\ell}^{\mathrm{ours}}$ with the smallest error

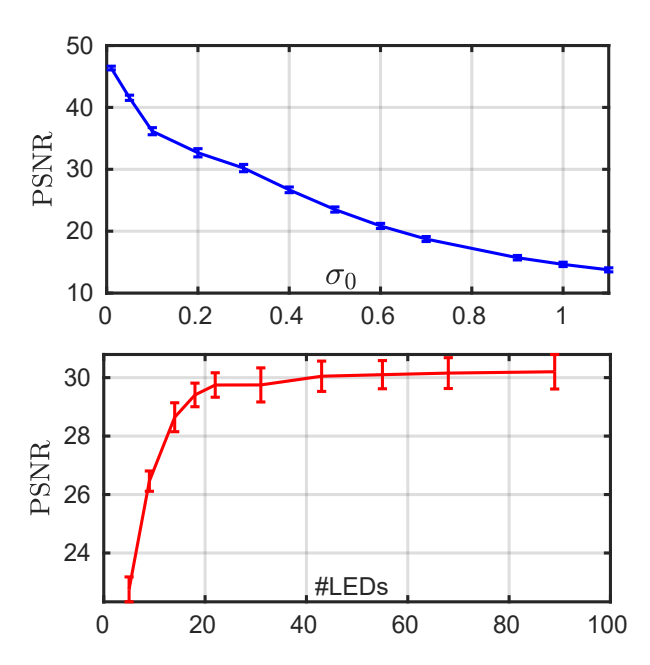
$$\hat{\ell} = \underset{\ell=\{1,2,3\}}{\operatorname{arg\,min}} \left\| \mathbf{y} - |\mathbf{F}\hat{\mathbf{o}}_{\ell}^{\text{ours}}|_{2}^{2} \right\|_{2}^{2}$$
 (175)

was used as the final estimate $\hat{o}_{\hat{\ell}}^{\mathrm{ours}}$. Tab. 2 and Fig. 17 show quantitative and qualitative results, respectively.

D.3. Fourier Ptychography: Real Experiment

In all experiments [41] that are used in Sec. 4.3 and inhere $\lambda = 512 \mathrm{nm}$ and NA = 0.2. For the configuration of M = 89 LEDs (see Fig. 12), the maximal LED angle is set such that the effective numerical aperture of the system is $3.1 \times \mathrm{NA}$.

Fig. 12 visualizes the measuring coverage for different numbers of LEDs of the object's Fourier space in these experiments. We show Fourier ptychography results for real-world publicly available amplitude-only biological sample [40]. Using a Fourier ptychography imaging system, the amplitude of a sample of stained dog stomach cells was recovered in high resolution [41]. We randomly divided the recovered sample into non-spatially overlapping patches, each of size 256×256 pixels. Then, the patches were split randomly into training and test sets. We train our denoiser over the training set, according to Appendix B. For each patch o in the test set, we simulate M noisy measurements y, each with a single LED. Figs. 19 and 20 show quantitative and qualitative results, respectively. Additionally, Fig. 21 shows qualitative recovery results of Fig. 8.



bars stand for the PSNR standard deviation.

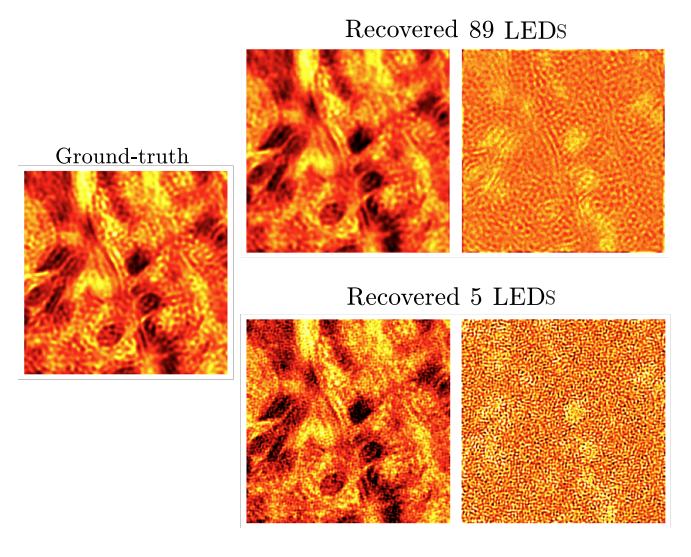


Figure 20. Qualitative results of amplitude objects. From left to right: Ground-truth image; Recovered images for M=5 and M=89Figure 19. The average PSNR of 10 amplitude-only objects: [Top] measurements; The difference between the true and estimated object. For different Poisson noise levels σ_0 with M=89. [Bottum] For a The dynamic range of the ground-truth and recovered images is [0,1]. varying number of LEDs M with a fixed noise level $\sigma_0 = 0.3$. The For better visualization, the dynamic range of both difference images is [-0.04, 0.04].

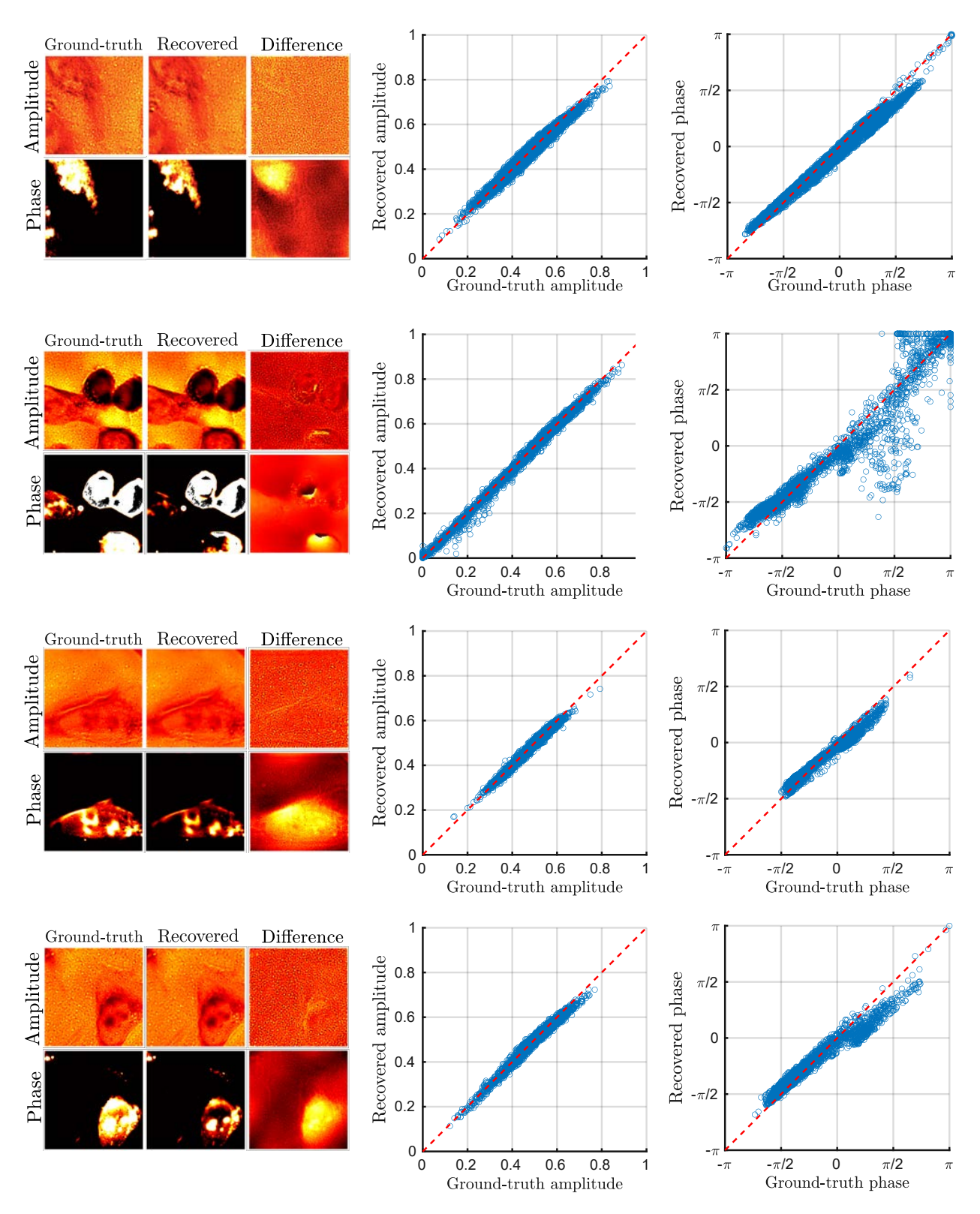


Figure 21. Fourier ptychography of complex-valued objects. Qualitative recovery results of four examples in our test set. Here, we used M=89 LEDs, a noise level of $\sigma_0=0.1$, and quantization using 8 bits per pixel. The dynamic range of the ground-truth and recovered images of the amplitude and phase is [0,1] and $[-\pi,\pi]$, respectively. For the difference images, the dynamic range is tuned just for visualization.

References

- [1] Emma Alexander, Leyla A. Kabuli, Oliver S. Cossairt, and Laura Waller. Depth from defocus as a special case of the transport of intensity equation. In *IEEE International Conference on Computational Photography (ICCP)*, pages 1–13, 2021.
- [2] Seung-Hwan Baek and Felix Heide. All-photon polarimetric time-of-flight imaging. In *Proceedings of the IEEE/CVF Conference on Computer Vision and Pattern Recognition (CVPR)*, pages 17876–17885, June 2022. 1
- [3] Yuval Bahat and Tomer Michaeli. Explorable super resolution. In *Proceedings of the IEEE/CVF Conference on Com*puter Vision and Pattern Recognition, pages 2716–2725, 2020. 2
- [4] Vivek Boominathan, Jesse K Adams, Jacob T Robinson, and Ashok Veeraraghavan. Phlatcam: Designed phase-mask based thin lensless camera. *IEEE transactions on pattern* analysis and machine intelligence (TPAMI), 42(7):1618– 1629, 2020. 1
- [5] Frank Bowman. *Introduction to Bessel functions*. Courier Corporation, 2012. 6, 14, 15
- [6] Dorian Chan, Srinivasa G Narasimhan, and Matthew O'Toole. Holocurtains: Programming light curtains via binary holography. In Proceedings of the IEEE/CVF Conference on Computer Vision and Pattern Recognition (CVPR), pages 17886–17895, 2022.
- [7] Shwetadwip Chowdhury, Michael Chen, Regina Eckert, David Ren, Fan Wu, Nicole Repina, and Laura Waller. High-resolution 3D refractive index microscopy of multiple-scattering samples from intensity images. *Optica*, 6(9):1211–1219, 2019. 1
- [8] Colin L. Cooke, Fanjie Kong, Amey Chaware, Kevin C. Zhou, Kanghyun Kim, Rong Xu, D. Michael Ando, Samuel J. Yang, Pavan Chandra Konda, and Roarke Horstmeyer. Physics-enhanced machine learning for virtual fluorescence microscopy. In *Proceedings of the IEEE/CVF International Conference on Computer Vision (ICCV)*, pages 3803–3813, October 2021.
- [9] James R Fienup. Phase retrieval algorithms: A comparison. *Applied optics*, 21(15):2758–2769, 1982. 8, 18, 21
- [10] Ian Goodfellow, Jean Pouget-Abadie, Mehdi Mirza, Bing Xu, David Warde-Farley, Sherjil Ozair, Aaron Courville, and Yoshua Bengio. Generative adversarial networks. *Communications of the ACM*, 63(11):139–144, 2020. 2
- [11] Javier Grau Chopite, Matthias B. Hullin, Michael Wand, and Julian Iseringhausen. Deep non-line-of-sight reconstruction. In Proceedings of the IEEE/CVF Conference on Computer Vision and Pattern Recognition (CVPR), June 2020. 2
- [12] Tao Huang, Songjiang Li, Xu Jia, Huchuan Lu, and Jianzhuang Liu. Neighbor2neighbor: Self-supervised denoising from single noisy images. In *Proceedings of the IEEE/CVF conference on computer vision and pattern recognition (CVPR)*, pages 14781–14790, 2021. 1
- [13] Rakib Hyder, Zikui Cai, and M Salman Asif. Solving phase retrieval with a learned reference. In European Conference on Computer Vision (ECCV), pages 425–441. Springer, 2020. 1

- [14] Zahra Kadkhodaie and Eero Simoncelli. Stochastic solutions for linear inverse problems using the prior implicit in a denoiser. Advances in Neural Information Processing Systems (NIPS), 34:13242–13254, 2021. 1, 3
- [15] Ulugbek S Kamilov, Ioannis N Papadopoulos, Morteza H Shoreh, Alexandre Goy, Cedric Vonesch, Michael Unser, and Demetri Psaltis. Learning approach to optical tomography. *Optica*, 2(6):517–522, 2015. 2
- [16] Bahjat Kawar, Gregory Vaksman, and Michael Elad. SNIPS: Solving noisy inverse problems stochastically. Advances in Neural Information Processing Systems (NIPS), 34:21757– 21769, 2021. 3, 4, 13
- [17] Bahjat Kawar, Gregory Vaksman, and Michael Elad. Stochastic image denoising by sampling from the posterior distribution. In *Proceedings of the IEEE/CVF International Conference on Computer Vision (ICCV)*, pages 1866–1875, 2021. 1, 3, 4, 7
- [18] Ken Kreutz-Delgado. The complex gradient operator and the CR-calculus. arXiv preprint arXiv:0906.4835, 2009. 16
- [19] Prashanth G Kumar and Rajiv Ranjan Sahay. Low rank poisson denoising (LRPD): A low rank approach using split bregman algorithm for poisson noise removal from images. In Proceedings of the IEEE/CVF Conference on Computer Vision and Pattern Recognition Workshops (WCVPR), pages 0–0, 2019.
- [20] Henry Oliver Lancaster and Eugene Seneta. Chi-square distribution. *Encyclopedia of biostatistics*, 2, 2005. 6, 14, 15
- [21] Axel Levy, Frédéric Poitevin, Julien Martel, Youssef Nashed, Ariana Peck, Nina Miolane, Daniel Ratner, Mike Dunne, and Gordon Wetzstein. CryoAI: Amortized inference of poses for ab initio reconstruction of 3D molecular volumes from real cryo-em images. In European Conference on Computer Vision (ECCV), pages 540–557. Springer, 2022. 2
- [22] David B Lindell, Dave Van Veen, Jeong Joon Park, and Gordon Wetzstein. BACON: Band-limited coordinate networks for multiscale scene representation. In *Proceedings of* the IEEE/CVF Conference on Computer Vision and Pattern Recognition (CVPR), pages 16252–16262, 2022. 2
- [23] David Martin, Charless Fowlkes, Doron Tal, and Jitendra Malik. A database of human segmented natural images and its application to evaluating segmentation algorithms and measuring ecological statistics. In *Proceedings Eighth IEEE International Conference on Computer Vision. ICCV 2001*, volume 2, pages 416–423. IEEE, 2001. 18
- [24] Christopher Metzler, Phillip Schniter, Ashok Veeraraghavan, et al. prdeep: Robust phase retrieval with a flexible deep network. In *International Conference on Machine Learning* (*ICML*), pages 3501–3510. PMLR, 2018. 9, 18, 21, 22
- [25] Christopher A Metzler, Arian Maleki, and Richard G Baraniuk. BM3D-PRGAMP: Compressive phase retrieval based on BM3D denoising. In 2016 IEEE International Conference on Image Processing (ICIP), pages 2504–2508. IEEE, 2016. 18
- [26] Shichong Peng and Ke Li. Generating unobserved alternatives: A case study through super-resolution and decompression. 2020. 2
- [27] Netanel Ratner and Yoav Y Schechner. Illumination multiplexing within fundamental limits. In *IEEE Conference on*

- Computer Vision and Pattern Recognition (CVPR), pages 1–8. IEEE, 2007. 1, 2
- [28] Albert W. Reed, Hyojin Kim, Rushil Anirudh, K. Aditya Mohan, Kyle Champley, Jingu Kang, and Suren Jayasuriya. Dynamic CT reconstruction from limited views with implicit neural representations and parametric motion fields. In Proceedings of the IEEE/CVF International Conference on Computer Vision (ICCV), pages 2258–2268, October 2021.
- [29] J. H. Rick Chang, Chun-Liang Li, Barnabas Poczos, B. V. K. Vijaya Kumar, and Aswin C. Sankaranarayanan. One network to solve them all – solving linear inverse problems using deep projection models. In *Proceedings of the IEEE International Conference on Computer Vision (ICCV)*, Oct 2017. 2
- [30] Gareth O Roberts and Richard L Tweedie. Exponential convergence of langevin distributions and their discrete approximations. *Bernoulli*, pages 341–363, 1996.
- [31] John Rodenburg and Andrew Maiden. Ptychography. Springer Handbook of Microscopy, pages 819–904, 2019. 1
- [32] Roi Ronen, Yoav Y Schechner, and Eshkol Eytan. 4D cloud scattering tomography. In Proceedings of the IEEE/CVF International Conference on Computer Vision (ICCV), pages 5520–5529, 2021. 1
- [33] Fahad Shamshad, Asif Hanif, Farwa Abbas, Muhammad Awais, and Ali Ahmed. Adaptive ptych: Leveraging image adaptive generative priors for subsampled fourier ptychography. In Proceedings of the IEEE/CVF International Conference on Computer Vision Workshops (WICCV), pages 0–0, 2019. 1
- [34] Yoav Shechtman, Yonina C Eldar, Oren Cohen, Henry Nicholas Chapman, Jianwei Miao, and Mordechai Segev. Phase retrieval with application to optical imaging: A contemporary overview. *IEEE signal processing magazine*, 32(3):87–109, 2015. 3
- [35] Mark Sheinin, Dorian Chan, Matthew O'Toole, and Srinivasa G Narasimhan. Dual-shutter optical vibration sensing. In *Proceedings of the IEEE/CVF Conference on Computer Vision and Pattern Recognition (CVPR)*, pages 16324–16333, 2022. 1
- [36] Lingfei Song, Lizhi Wang, Min H Kim, and Hua Huang. High-accuracy image formation model for coded aperture snapshot spectral imaging. *IEEE Transactions on Computational Imaging*, 8:188–200, 2022. 1
- [37] Yang Song and Stefano Ermon. Generative modeling by estimating gradients of the data distribution. Advances in Neural Information Processing Systems (NIPS), 32, 2019.
- [38] Yang Song and Stefano Ermon. Improved techniques for training score-based generative models. Advances in neural information processing systems (NIPS), 33:12438–12448, 2020. 4, 6
- [39] Kenichiro Tanaka, Yasuhiro Mukaigawa, and Achuta Kadambi. Polarized non-line-of-sight imaging. In *Proceedings of the IEEE/CVF Conference on Computer Vision and Pattern Recognition (CVPR)*, June 2020. 1
- [40] Lei Tian, Xiao Li, Kannan Ramchandran, and Laura Waller. (Dataset) LED array 2D Fourier Ptychography. Available

- online. http://gigapan.com/gigapans/170956.
 8.9.22
- [41] Lei Tian, Xiao Li, Kannan Ramchandran, and Laura Waller. Multiplexed coded illumination for Fourier ptychography with an led array microscope. *Biomedical optics express*, 5(7):2376–2389, 2014. 1, 8, 9, 17, 22
- [42] Weixi Wang, Ji Li, and Hui Ji. Self-supervised deep image restoration via adaptive stochastic gradient langevin dynamics. In Proceedings of the IEEE/CVF Conference on Computer Vision and Pattern Recognition (CVPR), pages 1989– 1998, 2022.
- [43] Max Welling and Yee W Teh. Bayesian learning via stochastic gradient langevin dynamics. In *Proceedings of the international conference on machine learning (ICML)*, pages 681–688, 2011.
- [44] Shumian Xin, Sotiris Nousias, Kiriakos N Kutulakos, Aswin C Sankaranarayanan, Srinivasa G Narasimhan, and Ioannis Gkioulekas. A theory of Fermat paths for nonline-of-sight shape reconstruction. In *Proceedings of the IEEE/CVF Conference on Computer Vision and Pattern Recognition (CVPR)*, pages 6800–6809, 2019. 1
- [45] Duoduo Xue, Ziyang Zheng, Wenrui Dai, Chenglin Li, Junni Zou, and Hongkai Xiong. On the convergence of non-convex phase retrieval with denoising priors. *IEEE Transactions on Signal Processing*, 70:4424–4439, 2022.
- [46] Guangming Zang, Ramzi Idoughi, Congli Wang, Anthony Bennett, Jianguo Du, Scott Skeen, William L Roberts, Peter Wonka, and Wolfgang Heidrich. TomoFluid: Reconstructing dynamic fluid from sparse view videos. In *Proceedings of* the IEEE/CVF Conference on Computer Vision and Pattern Recognition (CVPR), pages 1870–1879, 2020. 1
- [47] Feilong Zhang, Xianming Liu, Cheng Guo, Shiyi Lin, Junjun Jiang, and Xiangyang Ji. Physics-based iterative projection complex neural network for phase retrieval in lensless microscopy imaging. In *Proceedings of the IEEE/CVF Conference on Computer Vision and Pattern Recognition (CVPR)*, pages 10523–10531, 2021. 1
- [48] Yongyi Zhao, Ankit Raghuram, Hyun K. Kim, Andreas H. Hielscher, Jacob T. Robinson, and Ashok Veeraraghavan. High resolution, deep imaging using confocal time-of-flight diffuse optical tomography. *IEEE Transactions on Pattern Analysis and Machine Intelligence*, 43(7):2206–2219, 2021.